remote sensing

MDPI

Article

Assessment of the Ground Vulnerability in the Preveza Region (Greece) Using the European Ground Motion Service and Geospatial Data Concerning Critical Infrastructures

Eleftheria Basiou [1], Ignacio Castro-Melgar [2,3,*], Haralambos Kranis [1], Andreas Karavias [2], Efthymios Lekkas [1] and Issaak Parcharidis [2]

[1] Department of Geology and Geoenviroment, National and Kapodistrian University of Athens, 15771 Athens, Greece; eleutheriaba@geol.uoa.gr (E.B.); hkranis@geol.uoa.gr (H.K.); elekkas@geol.uoa.gr (E.L.)
[2] Department of Geography, Harokopio University of Athens, 17676 Athens, Greece; karavias@hua.gr (A.K.); parchar@hua.gr (I.P.)
[3] Institute of Geophysics, Czech Academy of Sciences, 14100 Prague, Czech Republic
* Correspondence: icastromelgar@ig.cas.cz

Abstract: The European Ground Motion Service (EGMS) and geospatial data are integrated in this paper to evaluate ground deformation and its effects on critical infrastructures in the Preveza Regional Unit. The EGMS, a new service of the Copernicus Land Monitoring Service, employs information from the C-band Synthetic Aperture Radar (SAR)-equipped Sentinel-1A and Sentinel-1B satellites. This allows for the millimeter-scale measurement of ground motion, which is essential for assessing anthropogenic and natural hazards. The study examines ground displacement from 2018 to 2022 using multi-temporal Synthetic Aperture Radar Interferometry (MTInSAR). The Regional Unit of Preveza was selected for study area. According to the investigation, the area's East–West Mean Velocity Displacement varies between 22.5 mm/y and −37.7 mm/y, while the Vertical Mean Velocity Displacement ranges from 16 mm/y to −39.3 mm/y. Persistent Scatterers (PSs) and Distributed Scatterers are the sources of these measurements. This research focuses on assessing the impact of ground deformation on 21 school units, 2 health centers, 1 hospital, 4 bridges and 1 dam. The findings provide valuable insights for local authorities and other stakeholders, who will greatly benefit from the information gathered from this study, which will lay the groundwork for wise decision-making and the creation of practical plans to strengthen the resistance of critical infrastructures to ground motion.

Keywords: critical infrastructures; Copernicus; EGMS; MTInSAR; Preveza

Academic Editors: Daniele Cirillo, Pietro Tizzani and Francesco Brozzetti

Received: 21 November 2024
Revised: 10 January 2025
Accepted: 13 January 2025
Published: 18 January 2025

Citation: Basiou, E.; Castro-Melgar, I.; Kranis, H.; Karavias, A.; Lekkas, E.; Parcharidis, I. Assessment of the Ground Vulnerability in the Preveza Region (Greece) Using the European Ground Motion Service and Geospatial Data Concerning Critical Infrastructures. *Remote Sens.* **2025**, *17*, 327. https://doi.org/10.3390/rs17020327

1. Introduction

Critical infrastructures describes a variety of physical resources, operations, and systems that are essential to maintaining the prosperity, security, and well-being of the European Union (EU) [1].

Natural disasters (such as earthquakes, floods, etc.) alongside long-term hazards related to physical deterioration have an impact on the Earth's surface and infrastructures [2]. Effective monitoring of ground motion is an essential part of catastrophe risk assessment and management. The integration of this type of data into operational processes in both the public and private sector going forward will inevitably result in better risk management and protection of the assets at the local, regional, and even pan-European levels. This improved monitoring may help to mitigate loss of life [3].

In 2017, in response to these needs, the Copernicus Land Monitoring Service authorized the launch of the European Ground Motion Service (EGMS) [4]. The EGMS provides a unique and comprehensive geographic dataset across Europe, specifically designed to measure ground motion at the millimeter scale, resulting from events like landslides, subsidence, tectonic effects, earthquakes, or volcanic phenomena. The measurements have an impact on the stability of buildings, infrastructure, slopes, and mining areas [5]. With millimeter accuracy, The EGMS offers continuous, dependable data on anthropogenic and natural ground motion over the participating nations in Copernicus and across national borders [6].

This research makes use of the EGMS to monitor and analyze ground motion with unprecedented accuracy. The EGMS utilizes Level-1 Single Look Complex (SLC) data products from the twin Sentinel-1A and Sentinel-1B satellites, which carry C-band Synthetic Aperture Radar (SAR) operating at a wavelength of approximately 5.5 cm (5.405 GHz) [7].

The primary land acquisition mode is the Interferometric Wide (IW) swath, which allows for either single-polarization (HH or VV) or dual-polarization (VV + VH or HH + HV) data, depending on the location [8]. Single-polarization SAR systems transmit and receive radar signals with the same polarization, either vertical (VV) or horizontal (HH). A SAR system with dual polarization can use one polarization (H or V) for transmission and two polarizations (HH and HV or VV and VH) for reception [9]. Repeat-pass space-borne SAR interferometry, particularly Interferometric Synthetic Aperture Radar (InSAR), has become a widely adopted technique for cost-effective and large-scale monitoring of surface deformation [10].

The application of InSAR has become increasingly popular for monitoring surface deformation due to its numerous advantages. Its versatility allows for effective use in a wide range of natural risk contexts such as landslides monitoring [11], deformation in volcanic regions [12–14], pre- and post-earthquake monitoring [15], co-seismic ground ruptures [16], geothermal fields [17], subsidence [18], and many more [19,20]. These capabilities make InSAR an invaluable tool for providing detailed, spatially comprehensive insights into natural hazards. With accuracy similar to classic geodetic methods, the InSAR approach offers continuous spatial information over wide areas (about 100 × 100 km for ERS and Envisat ESA's satellites) [21].

The EGMS applies Multi-Temporal Satellite Interferometry (MTInSAR) techniques. MTInSAR uses an extensive stack of radar images to generate time series at precise measurement points. These points can include both Distributed Scatterers (DSs) and Persistent Scatterers (PSs) [22]. When applicable, DSs will be detected and used as measurement points (MPs) to expand the spatial coverage of the data in non-urban areas, based on the density of PSs and their average phase coherence [23]. The PSs are typically found above exposed rocks, over buildings, antennas, poles, and other objects, as well as in urban and industrial regions [24]. The DSs can be found, for example, in desert areas, strewn peaks, uncultivated fields, places covered with rubble, etc. The use of advanced algorithms developed by a consortium of four InSAR Processing Entities (IPEs)—including Persistent Scatterer Pair (IPP), SqueeSAR, Ground Stable Target Interferometry (GSAR-GTSI), and the Integrated Wide Area Processor (IWAP)—further enhances the spatial and temporal resolution of ground motion monitoring [25].

The present research focuses on ground deformation in the Regional Unit of Preveza (Greece), analyzing vertical and east–west displacement utilizing measurement points derived from the EGMS from 2018 to 2022. The primary objective is to assess the correlation between ground motion and critical infrastructures in the Regional Unit of Preveza, integrating EGMS data with geospatial information on critical infrastructures. The secondary

objective is to identify vulnerabilities in critical infrastructures that are related to ground motion assisting in the creation of efficient risk-reduction plans.

2. Materials and Methods

2.1. Case Study

The Regional Unit of Preveza, located in the region of Epirus in Northwestern Greece, was selected as the study area (Figure 1a). According to the data from the 2021 population census, Preveza has a total population of 54,681 residents. This information is derived from the official census, which aims to accurately record the population and collect demographic data, contributing to the study and analysis of demographic trends in the region. The population density of the Regional Unit is 52.75/km^2 and the capital city of Preveza has 19,308 inhabitants [26].

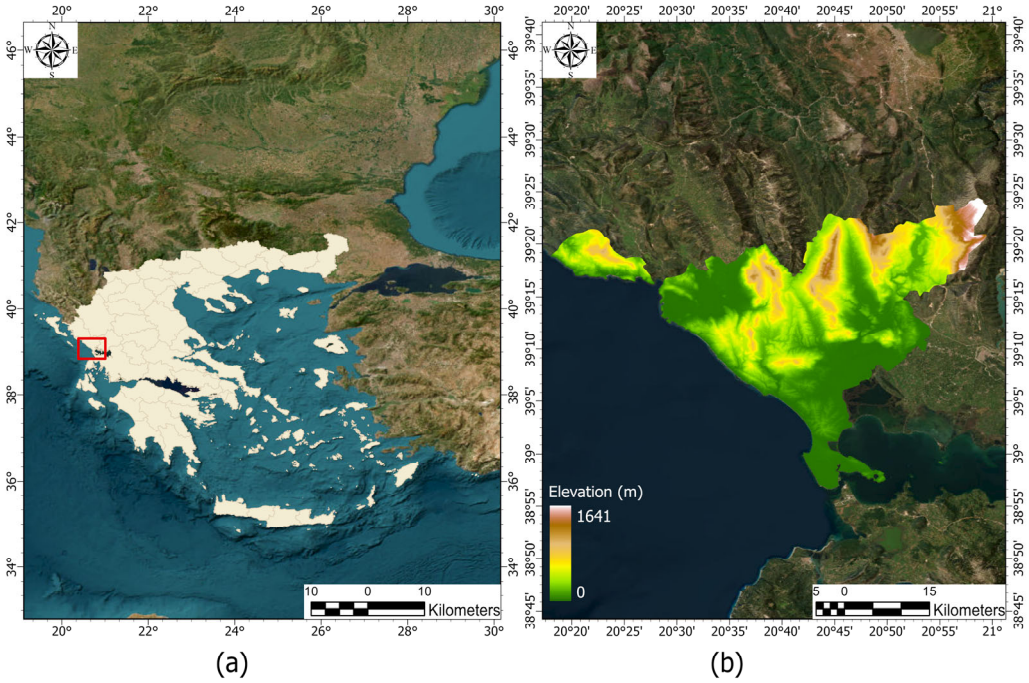

Figure 1. (**a**) Map of Greece with the Regional Unit of Preveza highlighted by a red square. (**b**) Elevation map of Preveza, where colors range from green (low elevations) to brown and white (higher elevations).

It covers a total area of 1037 square kilometers and is bordered to the northwest by the Regional Units of Ioannina and Thesprotia, to the east by the Regional Unit of Arta and the Amvrakikos Gulf, and to the west by the Ionian Sea. The elevation in Preveza ranges from sea level to a maximum of 1641 m (Figure 1b), with the coastal areas exhibiting lower altitudes and the northern and northeastern regions characterized by higher elevations. In Northwestern Greece, where Preveza is located, there is a transitional zone between the Inner Aegean extensional region and the outer compressional zone, and it exhibits a complex tectonic pattern [27]. Numerous notable faults are located in this region. The primary faults in Northwest Greece from north to south are as follows: Konitsa oblique-slip fault, Hani Dhelvinaki reverse strike-slip fault, Mitsikeli oblique-slip fault, Nerochori–Vrosina strike-slip fault, Petousi–Souli strike-slip fault, Variadhes strike-slip fault, Pesta oblique-slip fault, Kokkinopilos–Arta strike-slip fault, Zaloggo–Ziros oblique-slip fault, Kamarina–Arta oblique-slip fault [28,29]. A succession of moderate-sized earthquakes with a primary event of Mw 5.7 (Figure 2) struck the western Greek region of Epirus on 21 March 2020 (00:49:51.8 UTC), close to the village of Kanallaki [30]. In the

previous century, destructive earthquakes with magnitudes M < 6.0 have rarely occurred in the Kanallaki region of Preveza. However, in the 19th century there was a significant earthquake [31]. Near the village of Dragani, 15 km north of Kanallaki, an earthquake occurred on 14 May 1895, at 39.42°N, 20.61°E, h = n, M = 6.3. Seventy-five people were killed and 96 houses collapsed [30] in the settlement of Dragoumi (currently Zervohori), which was devastated [32].

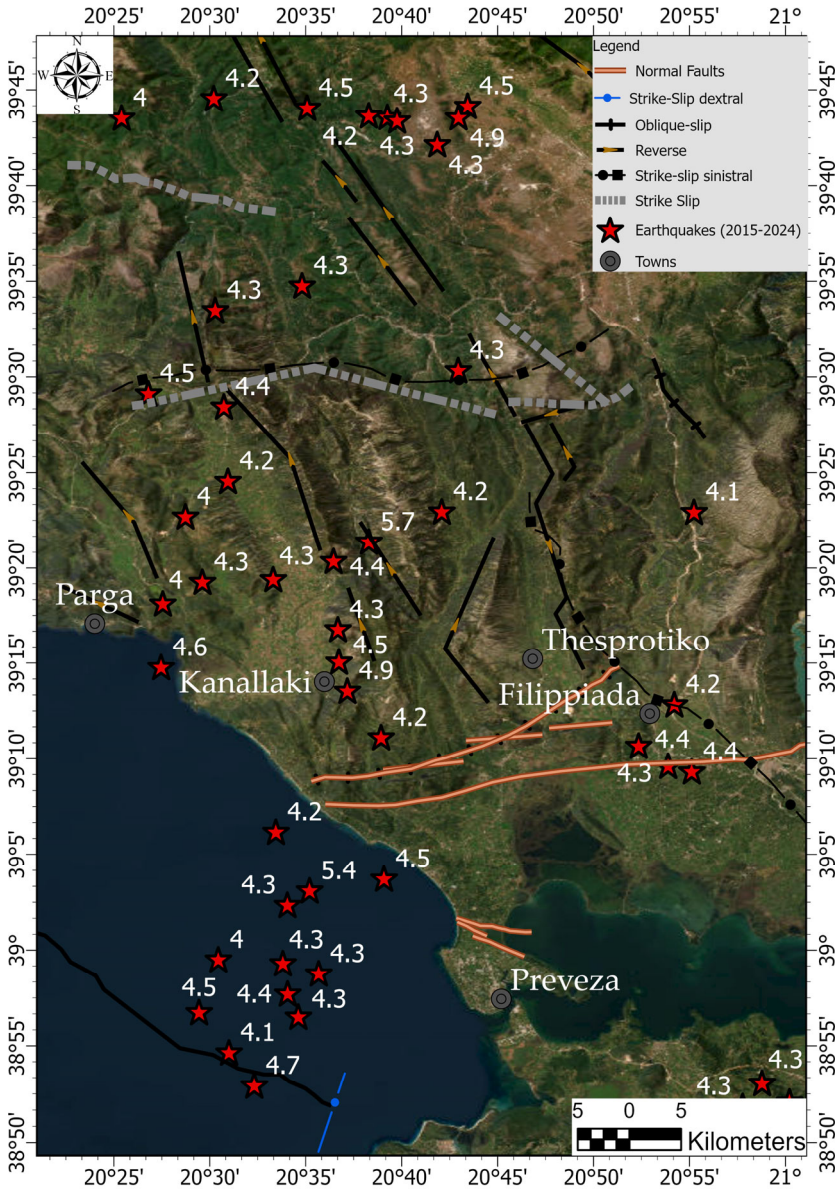

Figure 2. Map of earthquakes with M > 4 from 2015 [33,34], faults.

The most recent national seismic hazard map has three seismic hazard zones identified by the New Seismic Code: I = 0.16 g, II = 0.24 g, and III = 0.36 g [35], which is being utilized for infrastructure and building seismic design, and was first released in 2000, updated in 2003, and has not been updated since [36]. The seismic risk for the entire region of Epirus is 0.24 g [37] which indicates a serious hazard to the population. The region of Epirus is characterized by active tectonics and significant seismic activity (Figure 2), making it a dynamic and complex area for geological studies. Since 2015, many earthquakes of magnitude Mw > 4 have occurred.

The area of Preveza presents a unique opportunity to monitor ground deformation and assess its potential impacts on infrastructure and natural resources. Furthermore, the variation in elevation across the prefecture allows for the analysis of ground motion across different geomorphological settings. The selection of Preveza for this study is driven by its seismic hazards and the presence of several critical infrastructures, which are potentially vulnerable to geodynamic processes such as tectonic movements, ground subsidence, and slope instability.

2.2. European Ground Motion and Products

The EGMS is an advanced remote sensing product developed as part of the European Union's Copernicus Earth observation program. The EGMS provides annual updates and is designed for a wide range of applications, including the monitoring of critical infrastructures such as dams, bridges, railways, and buildings by municipal, regional, and national administrations. The service offers three product levels each tailored for specific monitoring requirements [5].

2.2.1. Baseline Products (L2a)

These products provide information on ground displacement derived from SAR in both ascending and descending orbits. At each measurement point, both detailed quality and position data are provided. The L2a products are referenced to a local reference point and are generated by independent processing of a single SAR data stack. These products are best suited for monitoring local movements [38].

2.2.2. Calibrated Products (L2b)

The L2b products offer more advanced data, calibrated using reference points from GNSS stations. [39] These products provide deformation measurements of the line of sight (LOS) of the satellite and incorporate information from both Differential Interferometry and GNSS stations. Due to the uneven distribution of GNSS stations across Europe, a 50 km grid velocity model is used to ensure consistent calibration across the dataset. This model helps to adjust the satellite-derived LOS velocities, improving the accuracy of the deformation measurements [40].

2.2.3. Ortho Products (Level 3)

The Level 3 products represent further enhancement, aimed at overcoming the limitations of the distortion in the LOS of the satellite, which is an obstacle to the interpretation of the results and their applications. By combining calibrated L2b products, the Ortho products offer separate measurements of vertical and horizontal (east–west) ground motion. Additionally, the Ortho products provide higher spatial resolution compared to the product levels, making them particularly valuable for detailed geospatial analysis [4].

2.3. Data and Software

The study utilized three primary InSAR products—basic product, calibrated product, and Ortho product—available from the EGMS for data visualization, analysis, and download [41]. The Level 3 Ortho products, which combine ascending and descending Level 2 LOS displacements to generate vertical (up–down) and horizontal (east–west) components of displacement [42], were analyzed over a five-year period from 2018 to 2022. The time series and velocities of absolute ground surface motions in both vertical and horizontal directions are the end products [43]. For the analysis, two datasets of Level 3 Ortho products were utilized, each with a sampling pace of six days for the period between January 2018 and December 2022. The datasets used include the files for east–west displacement and vertical displacement [40]. These datasets contain a CSV, an XML header file, and a

tiff file. The CSV files include attributes in the header, with each record representing a measurement point [43]. Every dataset utilized in this study contains 301 acquisition dates for both the vertical deformation product and the east–west deformation product for the timeframe 2018–2022. The spatial resolution of the InSAR data used in this study ranges between 5 and 20 m, depending on the scatterer density in the analyzed area. For urban areas (around 5 m resolution), the measurement point density is thousands per square kilometer, whereas for non-urban areas, it can reach hundreds per square kilometer [3]. The locations of the critical infrastructures (schools, hospitals, health centers, bridges, dams) were verified using Google Earth and verified sources [44]. The elevation data were derived from NASA's Shuttle Radar Topography Mission (SRTM) Global 1 Arc Second dataset, providing a homogenous 30 m resolution for the area [45]. For data visualization and mapping, ArcGIS Pro Software v. 3.3.2 [46] was employed. This desktop GIS software offers advanced tools for spatial data management, analysis, and cartographic visualization, enabling the creation of detailed maps of measurement points and infrastructure in the study area.

2.4. Process

The workflow can be seen in Figure 3. The dataset used for this study was selected based on the area of interest (AOI) corresponding to the Regional Unit of Preveza, covering the timeframe 2018–2022. The measurement points from the EGMS Ortho product (vertical and east–west displacement) were processed; the CSV file was processed and visualized after extracting the relevant data from EGMS CSV files. The mean velocity values of the ground surface movements were derived from these data and represented spatially (Figures 4 and 5) [43].

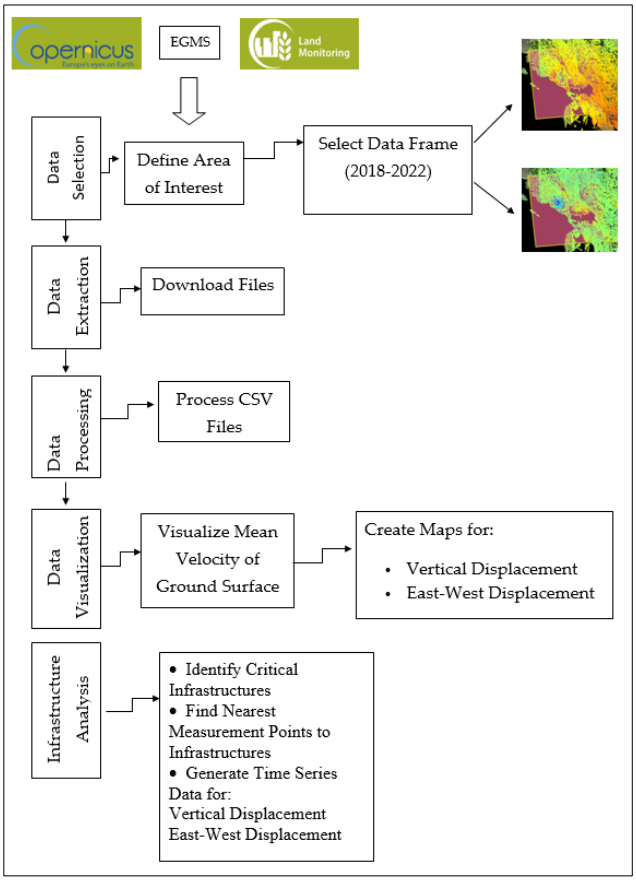

Figure 3. Workflow chart.

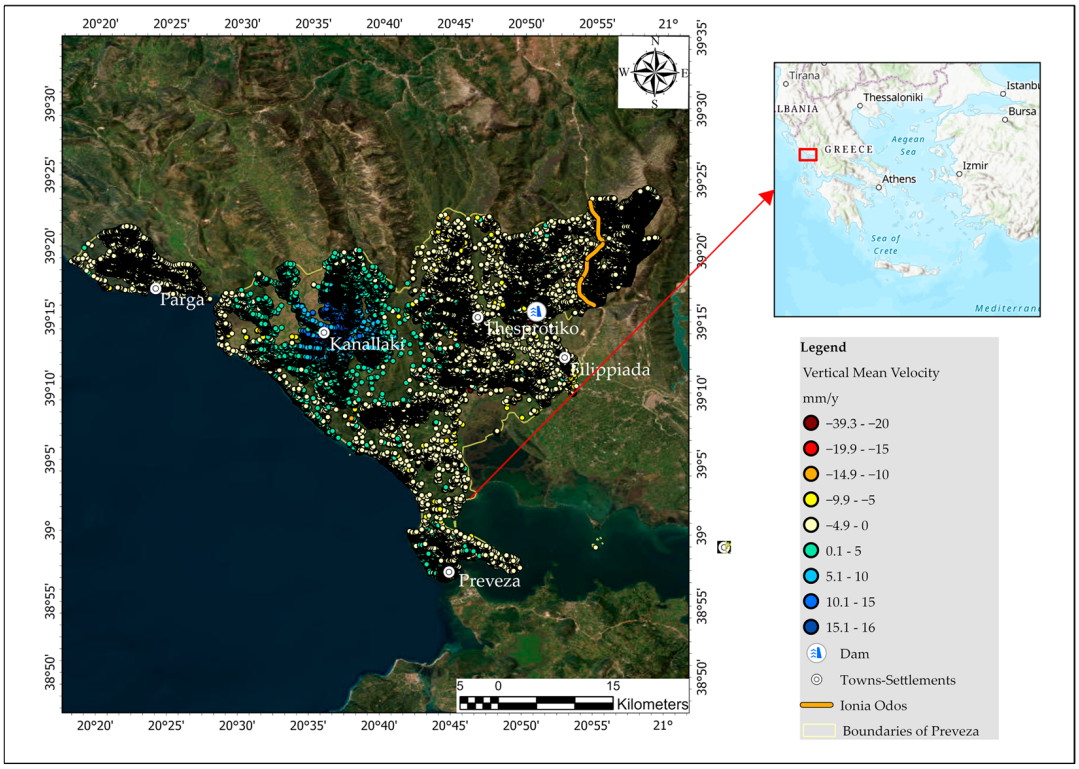

Figure 4. Measurement points of AOI, vertical displacement (mm/y), data: EGMS. The dark red is the maximum subsidence (−39.3 mm/y), light yellow is relatively stable, and dark blue is the maximum elevation.

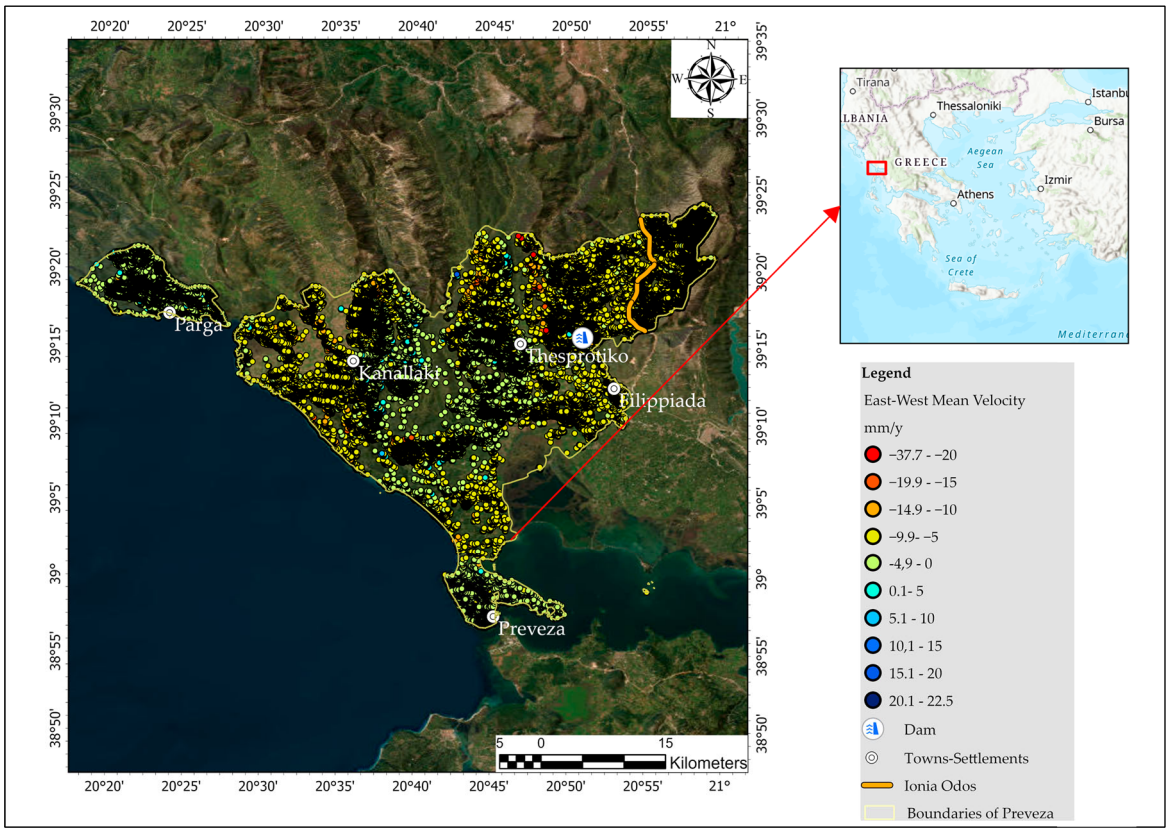

Figure 5. Measurement points of AOI, east–west displacement (mm/y), data: EGMS. The dark red. (−37.7 mm/y) is the maximum westward movement, light green is a stable horizontal motion, and dark blue is the maximum eastward movement (22.5 mm/y).

For each critical infrastructure within the study area, the nearest measurement point was identified to generate time series data for both vertical and east–west displacements (Tables A1–A4 in Appendix A). This allowed for a detailed trend analysis of ground motion across the study period (2018–2022), enabling an assessment of the impact of ground deformation on key infrastructures.

3. Results

Positive values in the vertical deformation velocity component indicate uplift or upward ground motion, while negative values reflect subsidence or downward displacement. Similarly, for the east–west deformation velocity component, positive values correspond to eastward displacement, whereas negative values signify westward movement. This distinction is crucial for interpreting the spatial patterns of ground motion and assessing the potential impact on critical infrastructures across the study area.

To better understand the final displacement of the area during the period 2018–2022, cumulative vertical (Figure 6) and east–west (Figure 7) displacement maps were generated, offering a detailed spatial representation of the motion patterns (Tables A5–A8 in Appendix B). These maps are presented alongside the geological map of the region (Figure 8) to provide a better contextualization of the results.

3.1. Kanallaki

For each critical infrastructure in this research, two time series were generated to represent the displacement of the nearest measurement point (MP): the time series that depicts the MP's vertical displacement over the period 2018–2022 and the time series that depicts the east–west displacement of the MP. Each of these time series provides a comprehensive representation of the ground motion in both directions for each MP, giving important information on the surface changes in close proximity of the critical infrastructure throughout the time period under research in the area of Kanallaki, five critical infrastructures, one health center, and four school units were studies (Figure 9). The time series of vertical displacement for the MP nearest to the health center shows values close to 0 mm until the middle of 2018. After that point, a small downward trend appeared with a minimum value of −5.7 mm in September 2018. Then, a period of recovery follows, during which values increase, subsidence reduces, and values are around 0 mm. After October 2019, a slight upward trend appeared in March 2020, where the displacement showed a significant and steep increase and values increased from 7.3 mm to 17.7 mm. After that time point, the values still increased at a slower pace, with the uplift trend reaching a maximum value of 26.8 mm in January 2022. Until the end of the 2022 dataset, the values decreased slightly at 14.1 mm, maintaining the uplift (Figure 10).

The time series for the east–west displacement of the health center is revealed in the time series of the vertical displacement values around 0 at first. After September 2018, a steady decrease began to appear in the values, showing westward movement and a steep change appeared in the vertical displacement specifically from −13 mm to −7 mm; following this, the downward shift returned with a steady pace, with small fluctuations, continuing westward movement until the value reached −18.7 by the end of the dataset. The event temporarily slowed the westward movement without stopping it. The health center has a cumulative vertical displacement of 14.1 mm and east–west displacement of −18.7 m.

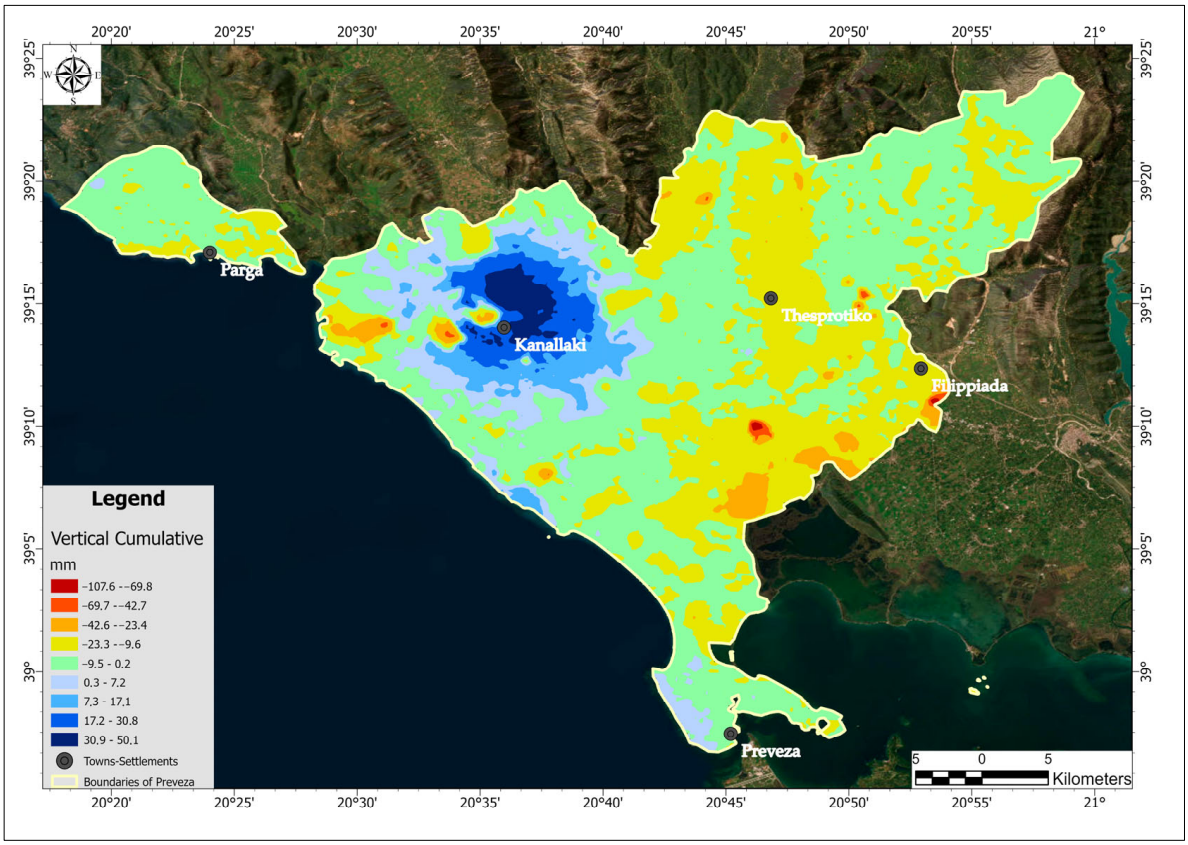

Figure 6. Vertical cumulative displacement region of Preveza.

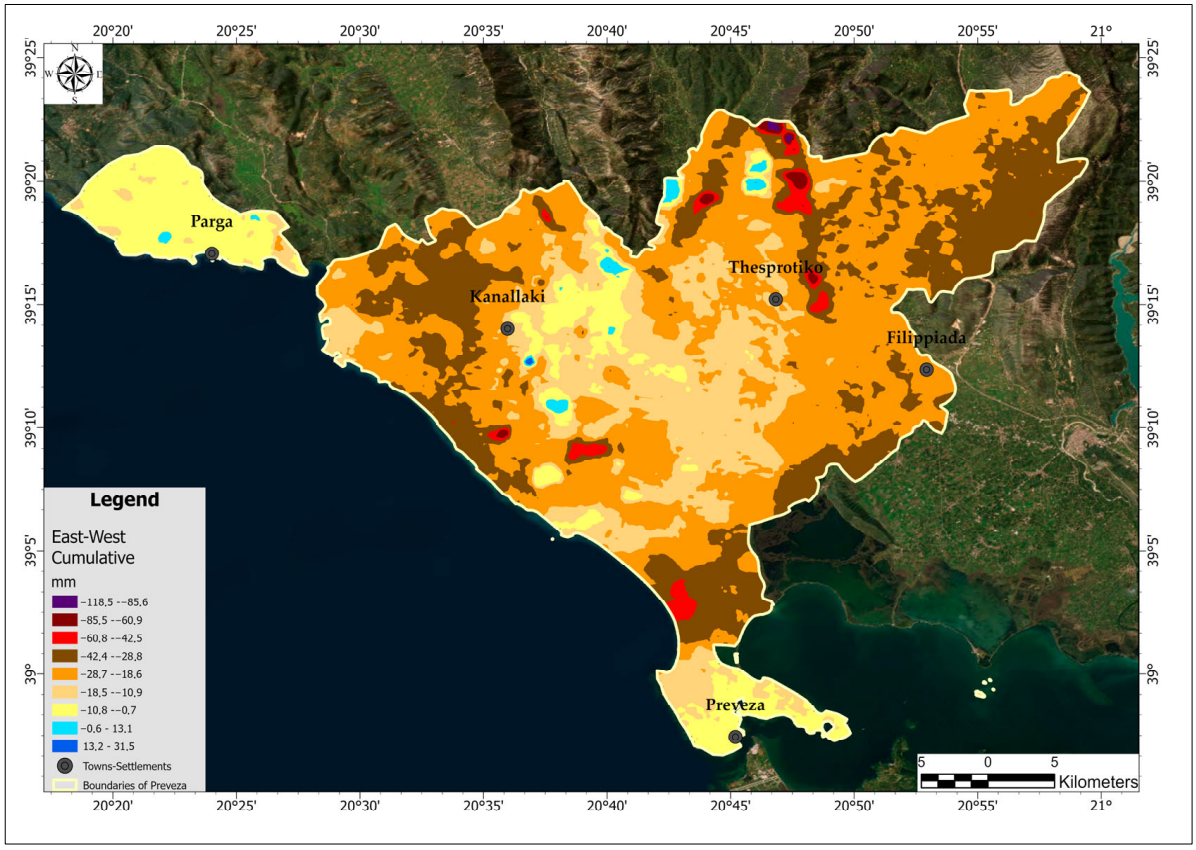

Figure 7. East–west cumulative displacement region of Preveza.

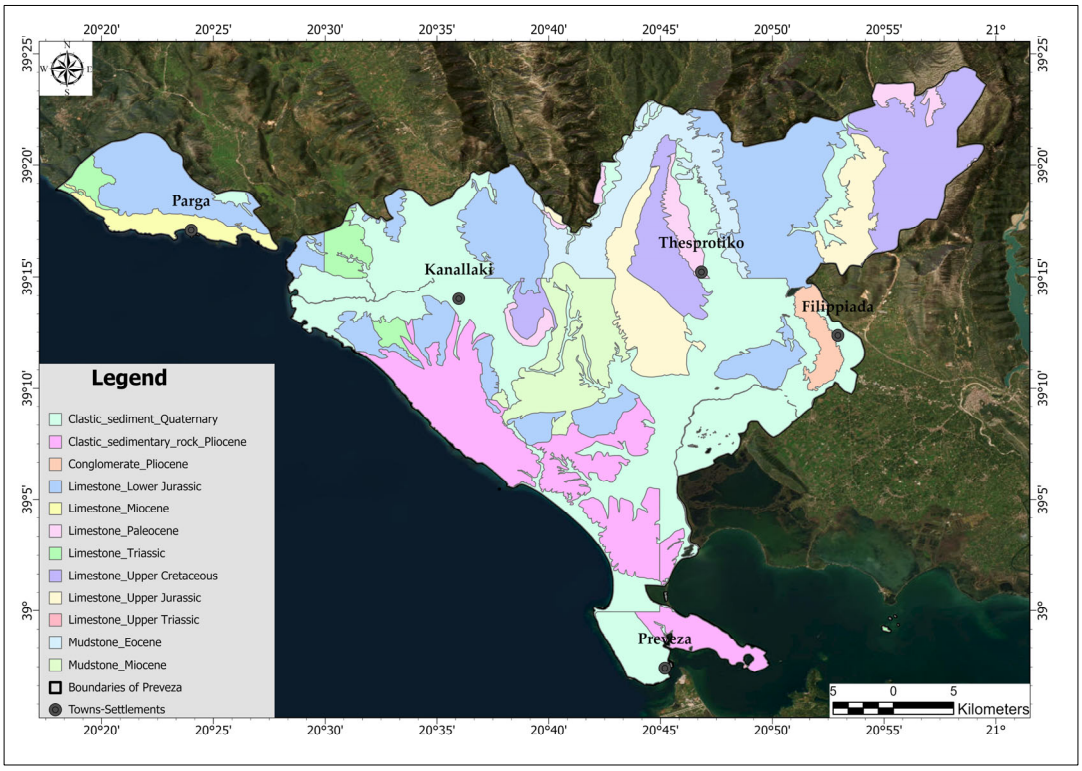

Figure 8. Geologic map of Preveza region.

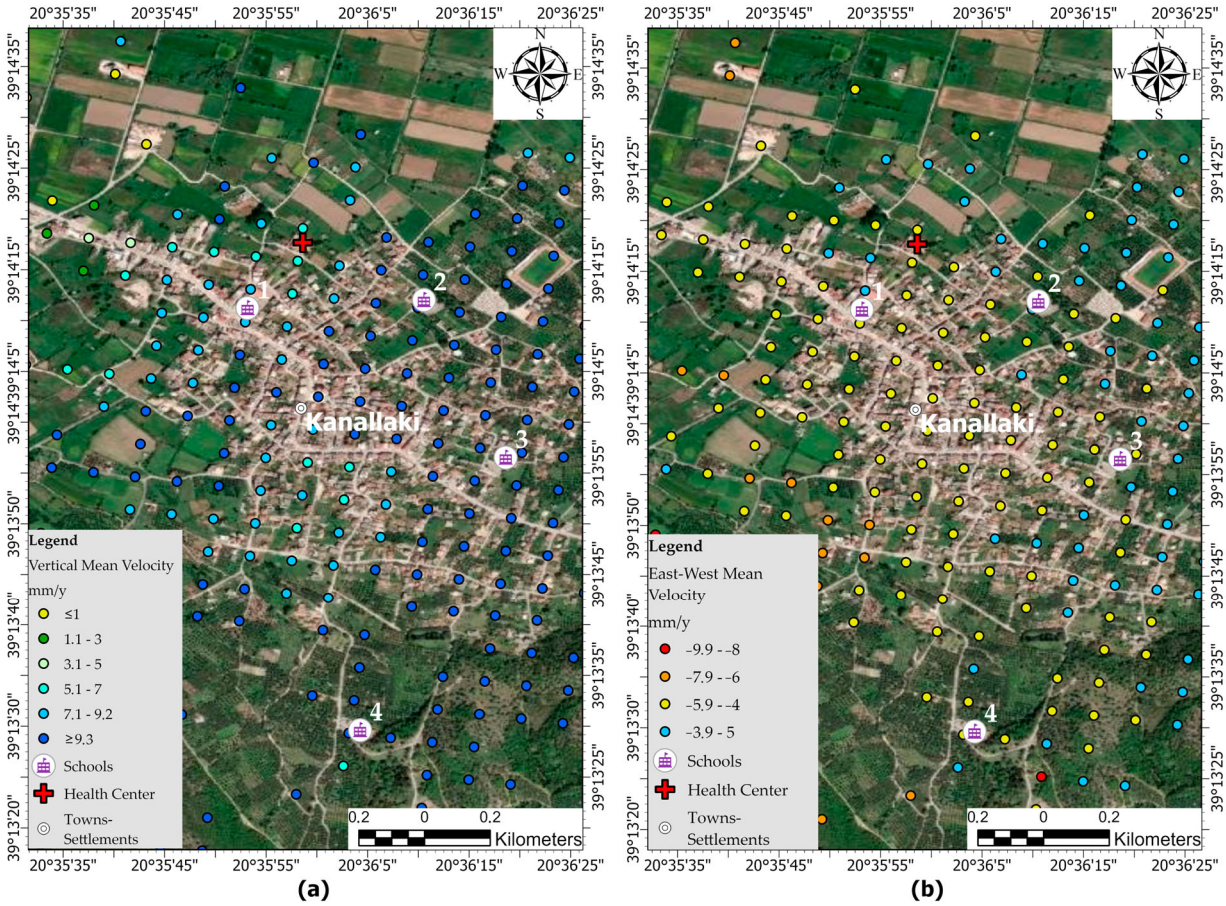

Figure 9. Area of Kanallaki, vertical (**a**) and east–west (**b**) displacement (mm/y), infrastructures (schools, health center).

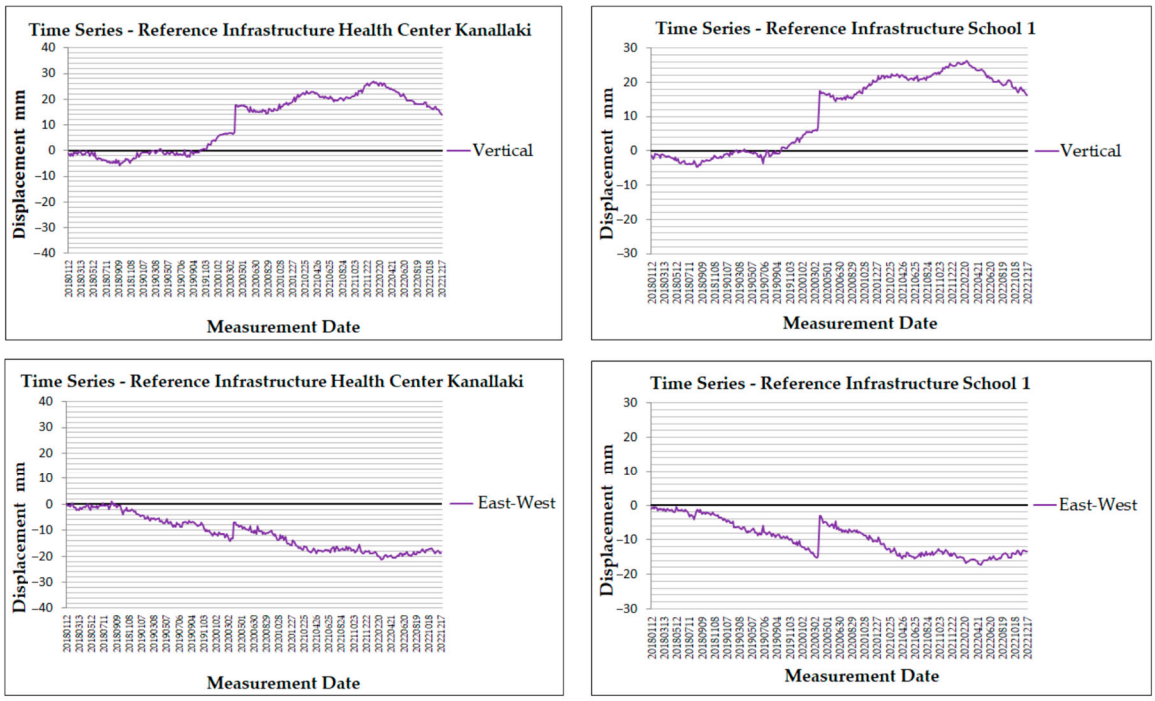

Figure 10. Time series for health center and School 1 in Kanallaki.

The vertical displacement time series for the MP near School 1 from the beginning of the dataset until September 2019 shows values from 0.4 mm to −4.7 mm. After this point, an uplift trend appears, increasing fast and reaching a critical transition, as in the previous time series, where the values suddenly increase in March 2020 from 6.8 mm to 17.5 mm. The uplift continues until the end of the dataset to reach the highest value of 26.2 mm in March 2022. By the end of the dataset, the values decrease slightly, settling at 16.1 mm. The westward motion of the MP for School 1 is marked on its time series, with consistently negative values from the start of the dataset. The point is moving fast towards the west until that time of point where the pace is slowed down and values change steeply from −14.7 mm to −3.1 mm in March 2020. The severe change in values is at the exact point of time as the vertical displacement. Although, in the vertical displacement, the course was not altered but maintained its course, in the east–west displacement, the course was altered instantly in order to return back to its previous path. School 1 has a cumulative vertical displacement of 16.1 mm and a cumulative east–west displacement of −13.5 mm (Figures 6 and 7).

Values from the vertical displacement times series of the MP for School 2 (Figure 11) have a similar range and pattern as the previous time series, which can be explained by the fact that the MP is located in the same area. The values range from 42 mm to −5.1 mm; subsidence is observed from the beginning of the dataset until February 2019, with values ranging from −0.2 mm to −5.1 mm. After that, values begin to increase, revealing an uplift with a few points in time having negative values. Notably, after August 2019, values are only positive with a steady increasing pace until it reaches the critical point of time in March 2020 where there is a significant increase in values from 7.9 mm to 30.4 mm. The uplift continues after that point to reach 42 mm in March 2022, maintaining similar values until the end of the dataset. A value of 33.6 mm is observed at the end of the period. The time series of the east–west displacement indicates a steady westward movement that reaches −14.7 mm in March 2020, and, in the next point, the values show a momentary sharp increase from −14.7 mm to −4.9 mm that caused the westward movement to slow down instantly. School 2 in Kanallaki reveals a cumulative vertical displacement of 33.6 mm,

a significant uplift combined with the cumulative east-west displacement of −15.1 mm (Figures 6 and 7).

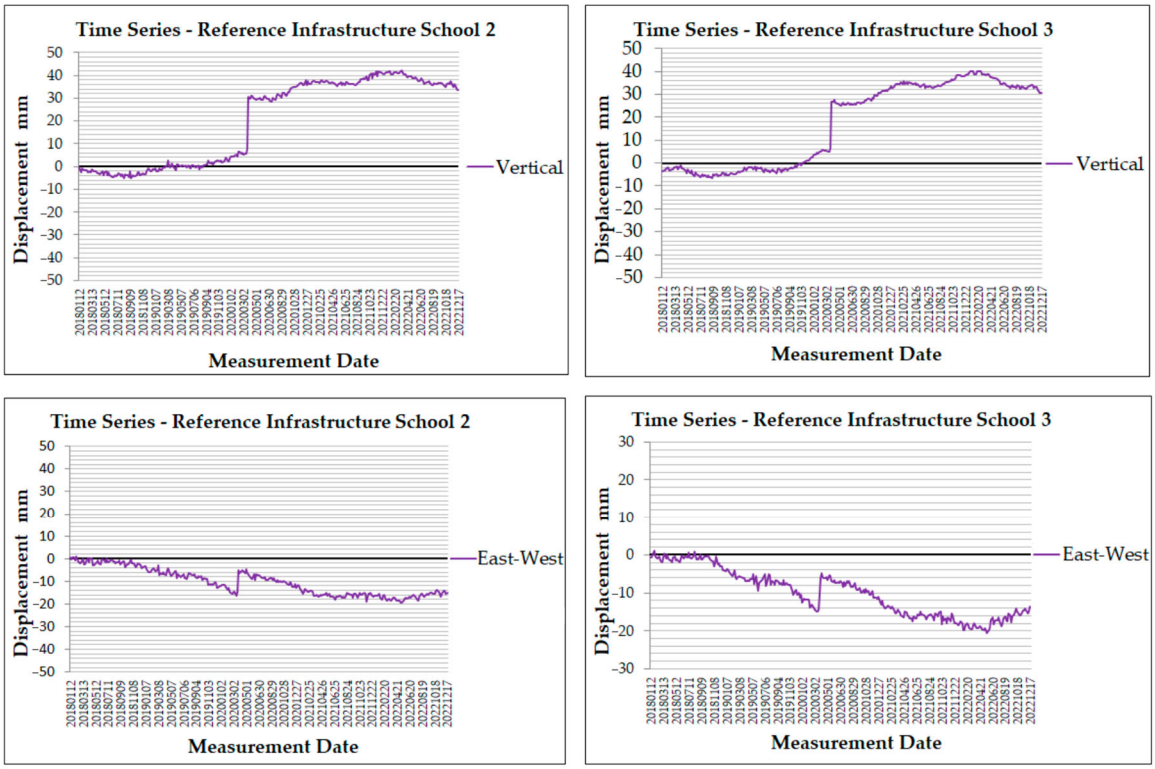

Figure 11. Time series for Schools 2 and 3 in Kanallaki.

The vertical displacement time series for the MP close to School 3 (Figure 11) presents a significant spike in values at a unique point in time. The values during the entire dataset range from 40.2 mm to −6.4 mm, representing one of the largest ranges of values observed in the time series that have been studied. From the beginning of the dataset until November 2019, there is a minor subsidence, with values ranging from −3.5 mm to −6.4 mm. After that point, an uplift appears, reaching 6.7 mm in March 2020. The next data point reveals a sudden increase in the values, indicating a critical event affecting displacement, with values from 6.7 mm to 26.7 mm (March 2020). After that critical point, the movement maintains an upward trend with a rather fast pace, reaching a maximum value of 40.2 mm in January 2022. Following this, a slight recovery begins, ending the dataset at 30.5 mm.

While the vertical displacement showed a sudden uplift, the east–west displacement also reveals a sudden change at the same time. At the initial time of the dataset values are relatively stable close to 0 mm until November 2018, ranging from 1.1 mm to −3 mm. Then, a downward shift is observed reaching the lowest value of −14.9 mm in March 2020. The next two points register similar values of −14.8 mm and −14.3 mm. At the same point in time, in the vertical displacement time series, values suddenly exhibited a sudden increase from −14.3 mm to −6.1 mm; this change slowed down the westward movement. During the remaining period, values return to their initial trend, revealing that the event only had a temporary effect. School 3 in Kanallaki has a similar pattern with a vertical cumulative displacement of 30.5 mm and cumulative east–west displacement of −13,7 mm (Figures 6 and 7).

The next vertical displacement time series shows the motion of the MP for School 4 (Figure 12). At the beginning of the period, subsidence is observed, with a trend of recovery. After September 2019, the values are consistently positive, indicating that an uplift has

begun to emerge. In this time series, a sudden spike is also observed in March 2020, with values rising sharply from 5.2 mm to 21.9 mm. This change is larger than the one observed for School 3. The uplift continues until the end of the dataset, ending with a value of 33 mm. The east–west displacement time series has a downward trend during the entire dataset, with values ranging from 0.2 mm to −23.1 mm. In March 2020, a similar steep change is observed, with values increasing from −16.7 mm to −8.9 mm. This change temporarily slows the westward movement before it resumes, reaching the lowest value of −23.1 mm in May 2022. School 4 presents a cumulative vertical value of 33 mm, with the cumulative east–west value of −17.9 mm (Figures 6 and 7).

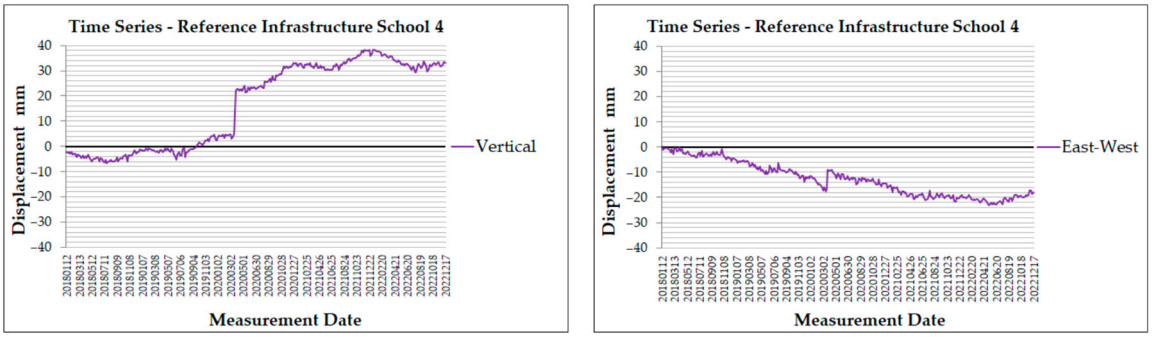

Figure 12. Time series for School 4 in Kanallaki.

3.2. Preveza

The time series for the MP close to the hospital of Preveza (Figure 13) shows variations in the vertical displacement mainly between −3.1 mm and 3.4 mm (Figure 14). The values are stabilized around 0 mm until the middle of 2019 but with slight fluctuations. Signs of a slight uplift are observed, not exceeding 3.4 mm, followed by a minor downward trend, especially toward the end of the period. The dataset ends with a value of −2.1 mm. In the east–west direction, the values are stable around 0 until 2019, after which a stable downward trend appears, reaching −10.9 mm by October 2021. From that point, until the end of the period, a slight recovery is observed, but the values remain negative, showing continued westward movement.

The time series for the MP close to the health center of Preveza indicates that the vertical displacement is stable, with values close to 0 mm, reaching a maximum of 3.4 mm in the year 2020 and a minimum of −2 mm in July 2022. The east–west displacement of the referenced infrastructure shows stable values around 0 mm until the beginning of 2019. After that, a clear downward trend is observed, reaching −10.7 mm at the end of October 2021, indicating a continued westward movement. At the end of the period, remain negative around −6 mm, with the dataset concluding at −5.5 mm.

The vertical displacement time series for the MP referenced for School 1 has a stable positive trend with values close to 0 mm (Figure 15) for most of the dataset period (2018–2022), with the highest value reaching 4.7 mm in September 2020. At the end of the time period, values appear slightly negative, reaching −1 mm in December 2022. The east–west displacement has a small positive displacement at the beginning, with values near 0 mm, revealing eastward motion. Slight fluctuations around 0 mm are observed initially, which suggests rather steady conditions. From 2019 until the end of the period (2022), the displacement follows negative values, indicating westward movement, with a minimum of −11.9 mm in August 2022.

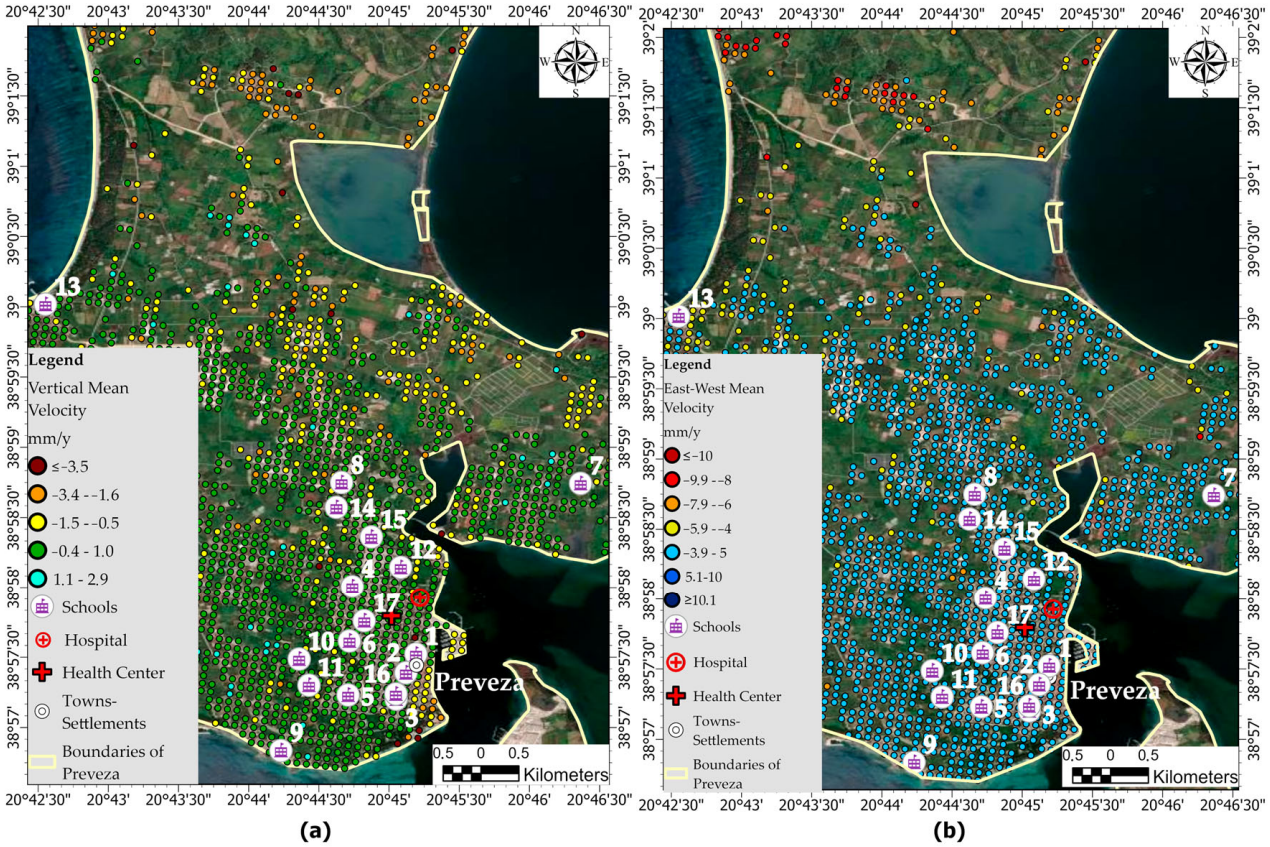

Figure 13. Area of Preveza, vertical (**a**) and east–west (**b**) displacement (mm/y), infrastructures (schools, hospital, health center).

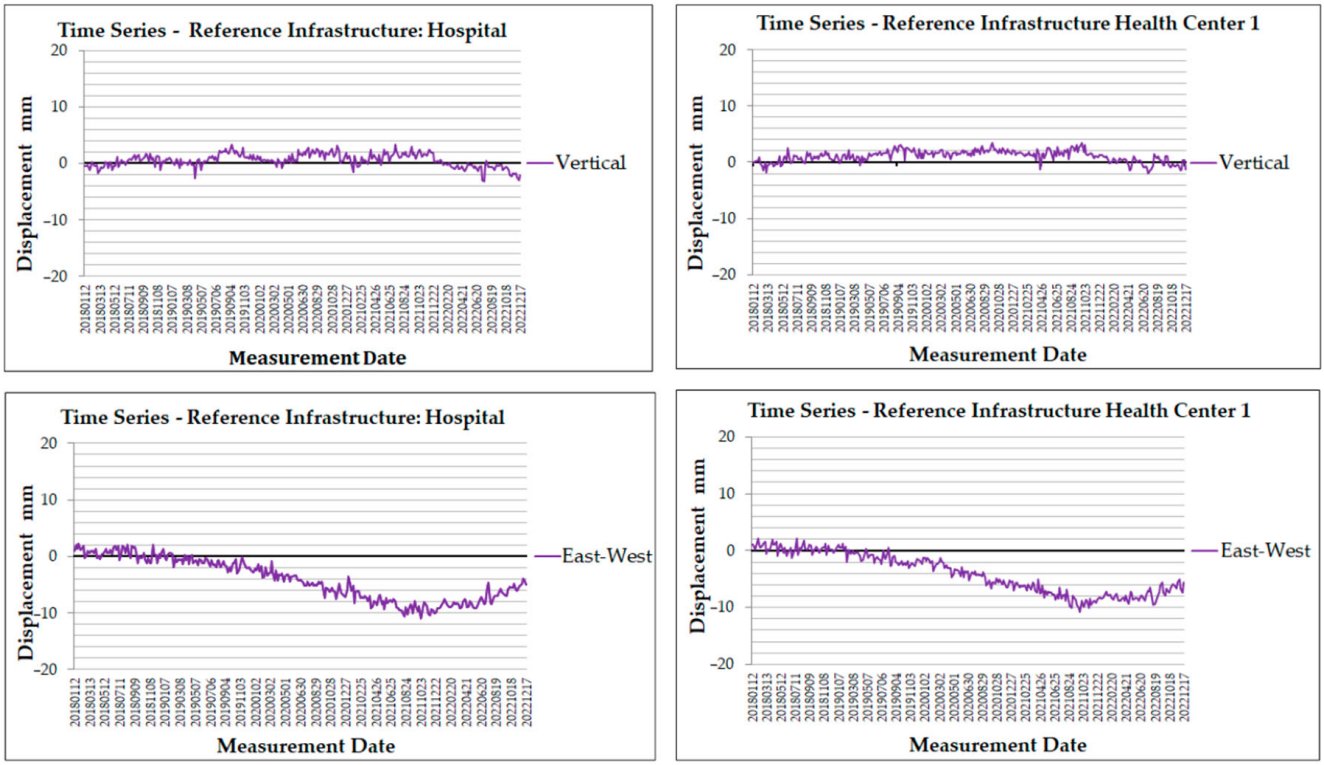

Figure 14. Times series for health infrastructures in area of Preveza.

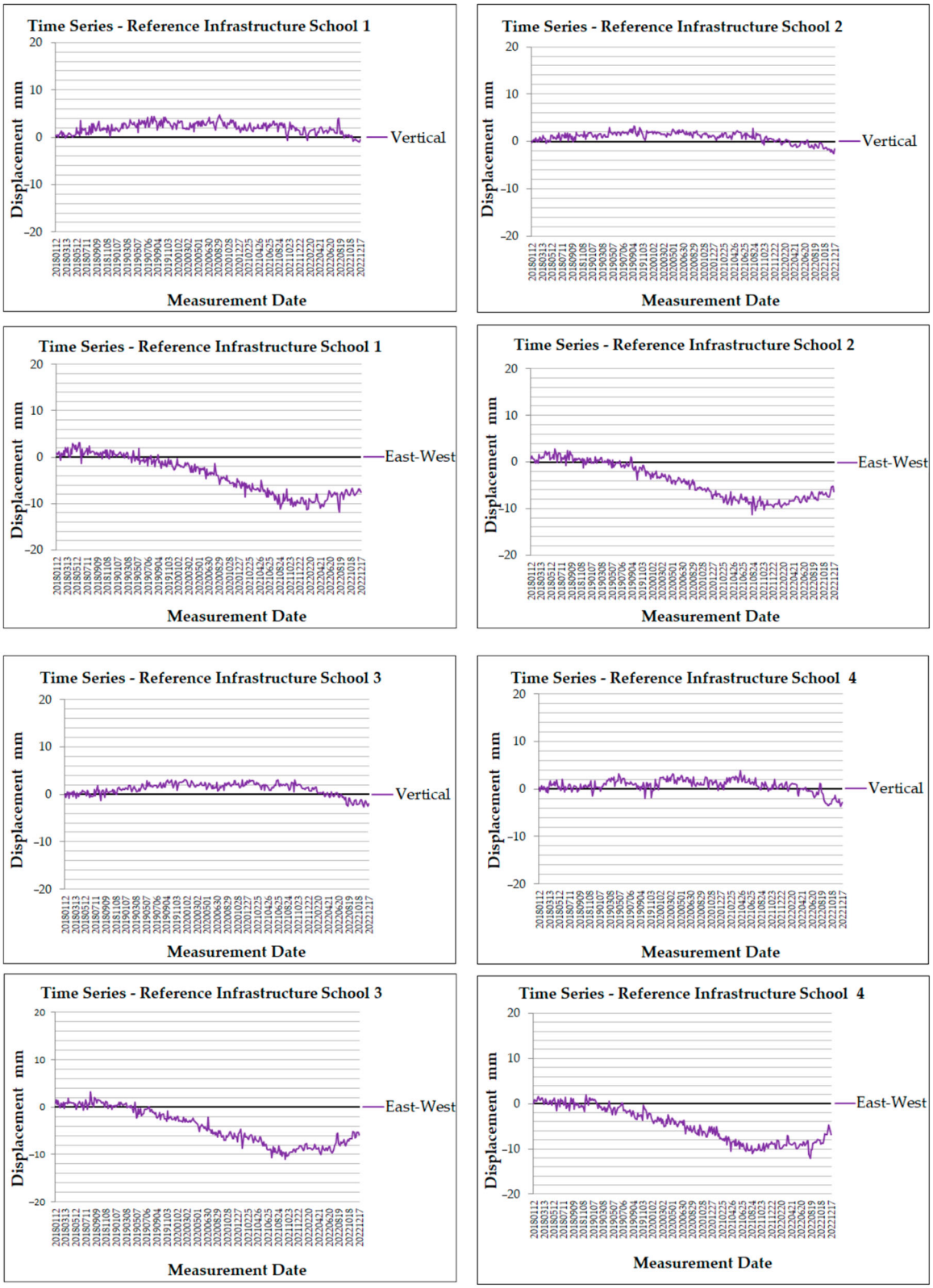

Figure 15. Times series for school infrastructures in area of Preveza (Schools 1–4).

The vertical displacement time series of the MP near School 2 appears to be a stable point with positive values that generally do not exceed 3.2 mm, indicating a slight uplift. Starting in 2021, some negative values appear, showing a minor trend towards subsidence, with values from 3.2 mm to −2.5 mm. In the east–west displacement time series, at the beginning of the dataset (2018), positive values prevail, indicating slow eastward movement.

After September 2019, only negative values appear, indicating westward movement. The entire dataset shows values from 2.8 mm to −11.3 mm. The dataset ends with a value of −6.4 mm.

The vertical displacement time series for the next MP, related to School 3, begins with very low values near 0 mm and continues with some fluctuations until the middle of 2022. There is a slight uplift until March 2022. After that point, a minimal decrease is observed, with the dataset ending at −1.9 mm. In the east–west displacement time series, values are initially mostly positive around 0 mm, with a maximum value of 3.2 mm in August 2018. Values range from 3.2 mm to −11 mm. From 2019, there is a downward trend where the displacement shows a rapid decrease, reaching a minimum of −11 mm at the end of 2021. After this period, values increase slightly but remain negative, indicating a westward shift in ground movement.

In School 4, the vertical displacement has values near 0 mm, suggesting no significant vertical movement in the MP. Minor fluctuations are observed, with the highest peak reaching 3.9 mm in April 2021 and the lowest value reaching −2.8 mm at the end of the dataset. Regarding the east–west displacement time series, fluctuations are more pronounced, with small peaks and a negative trend from the year 2019. Towards the end of the timeline, values reach −12.1 mm in August 2022. After approaching the minimum value, the data indicates a minor recovery towards zero, suggesting a slowing of the westward movement.

The vertical displacement for the MP for School 5 (Figure 16), like the previous one, is stable. For most of the dataset period, values remain positive, with the highest value of 2.8 mm in October 2019. Towards the end of the timeline, particularly in late 2022, the lowest value reaches −2.8 mm. The east–west displacement indicates a more significant movement with a faster pace. At the beginning of the dataset, the movement is eastward, with generally positive values in 2018 and a peak of 1.7 mm in June 2018. After that point, a downward movement is observed, reaching a minimum of −11.6 mm in May 2022. The MP shows a stable westward movement until the end of the period.

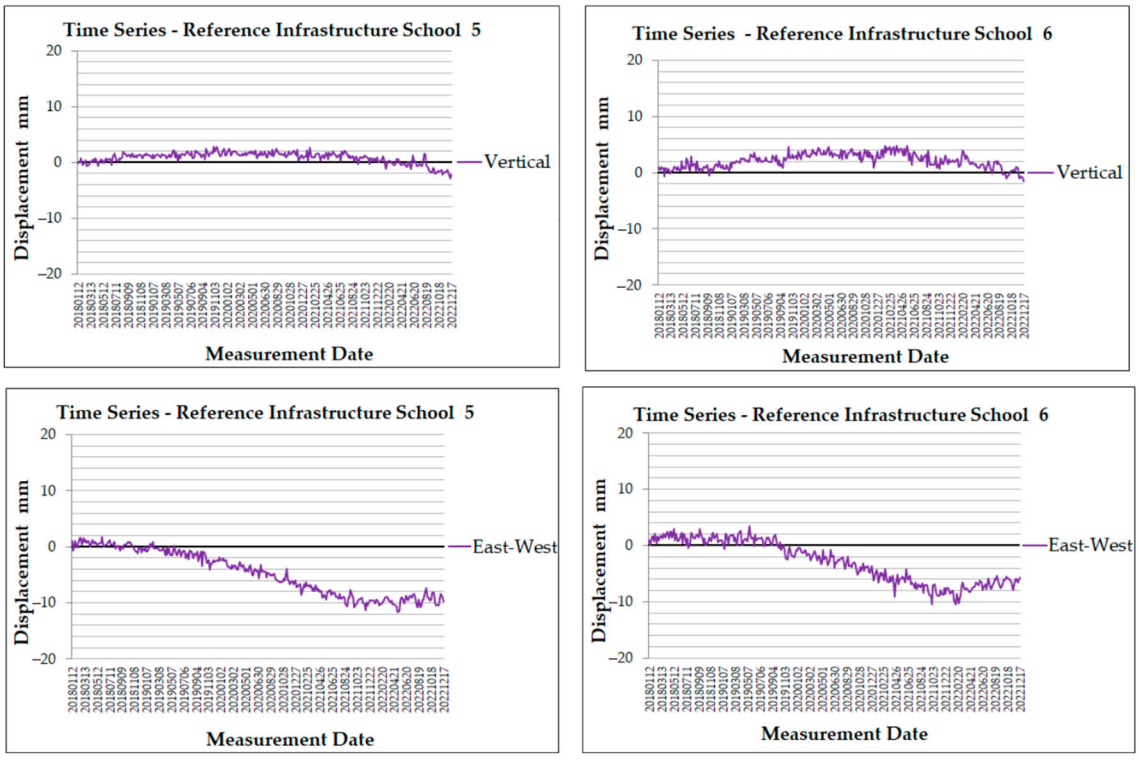

Figure 16. Times series for school infrastructures in area of Preveza (Schools 5–6).

Vertical displacement time series for MP near School 6 indicates numerous small fluctuations throughout most of the dataset. At the beginning of February 2021, the highest value is 4.8 mm, with fluctuations remaining after that point. Towards the end of the timeline, slight subsidence is observed, not exceeding −1.5 mm. In assessing the east–west displacement, it is observed that from the beginning of the dataset until 2019, the point remains stable around zero, with generally positive values not exceeding 3.4 mm, reaching a peak in May 2019, indicating a movement towards the east. After 2019, values are only negative, reaching a minimum of −10.4 mm in October 2021 and at the beginning of February 2022. The MP is moving towards the west with values around −5 mm. The end of the dataset concludes with a value of −5.7 mm.

In the time series for the MP that concerns School 7, there is a significant variation throughout the dataset, with alternating periods of uplift and subsidence occurring at a fast pace. In the first year, values range around 0, with the highest value reaching 4.8 mm at the end of October 2018. After that point, a sharp downward trend follows, with values approaching −4 mm at the beginning of 2019. Fluctuations continue until mid-2020, when a sudden peak in subsidence is observed, reaching −7.3 mm in June 2020. Subsequent upward and downward displacements take place, with the highest value of 5.4 mm in August 2021. The end of the time period indicates subsidence, reaching −5.9 mm. In the east–west time series, excluding the first quarter where some high values appear, including a peak of 3.5 mm, a table downward trend is observed. In the middle of June 2020, there is a sharp change, coinciding with the vertical displacement series, reaching −15.6 mm and causing a rapid westward shift. After that point, the movement towards the west continues stably with minor fluctuations, reaching a minimum of −16 mm in August 2021. By December 2022, values reach −9.7 mm, indicating continued westward movement.

The time series of the MP for School 8 (Figure 17) shows variations, but sharp peaks are not detected. There is a minor instability during the entire dataset that is revealed with small troughs that indicate uplifts and subsidence. The first half of 2018 is stable, with values around 0. Values range from 3 mm to −5.4 mm, ending the dataset at −3.7 mm.

In the east–west displacement time series, values are generally positive until the end of 2019, revealing a movement towards the east, with a range from 3.7 mm to −14 mm. At the end of 2019, a steady downward trend appears, indicating westward movement, culminating at −14 mm. After that, a small ascend occurs, not exceeding −6.9 mm at the end of the period.

From the beginning, the MP for School 9 shows only positive values and generally presents a stable uplift that does not exceed 5.7 mm (end of 2020). Values range from 5.7 mm to −0.3 mm during the dataset, ending with a value of 3.1 mm. The east–west time series is stable until the middle of 2019, after which a steady downward trend appears, demonstrating westward movement. The minimum value of −12.1 mm occurs in August 2018. After that, a small increase is observed, reaching −9.1 mm at the end of 2022, though the westward movement persists.

The time series of the MP near School 10 (Figure 18) reveals a general slight uplift during the dataset, with a few points indicating a slight subsidence. At the start, displacement values are stable around zero; after the end of 2018, there is a slight increase in values with minor fluctuations. In October 2021, the displacement reaches its highest value of 6.5 mm, and its lowest value of −0.5 mm on September 2022. The end of the period (December 2022) reveals an uplift with a value of 2 mm. The east–west displacement exhibits the opposite trend to the vertical displacement. Initially, values are stable at around 0; however, after August 2019, a steady downward trend appears, indicating the westward movement of the MP, with a minimum value of −11.4 mm observed in September 2022.

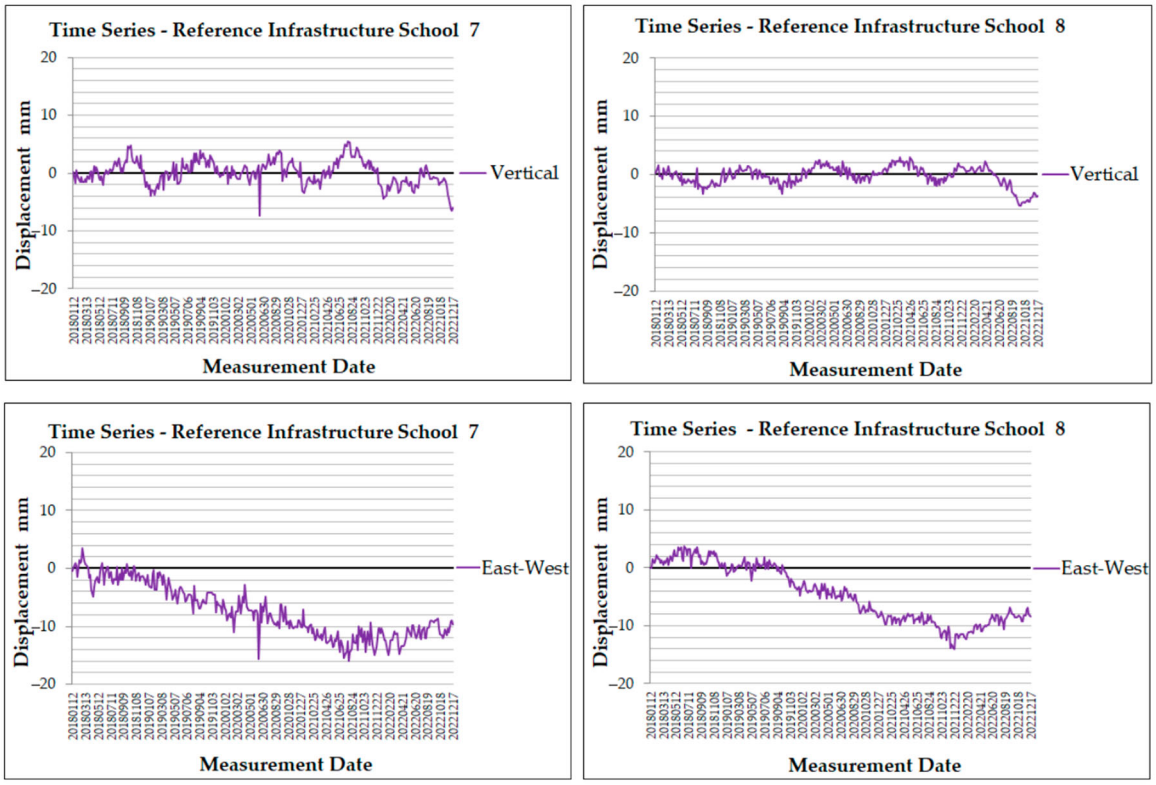

Figure 17. Times series for school infrastructures in area of Preveza (Schools 7–8).

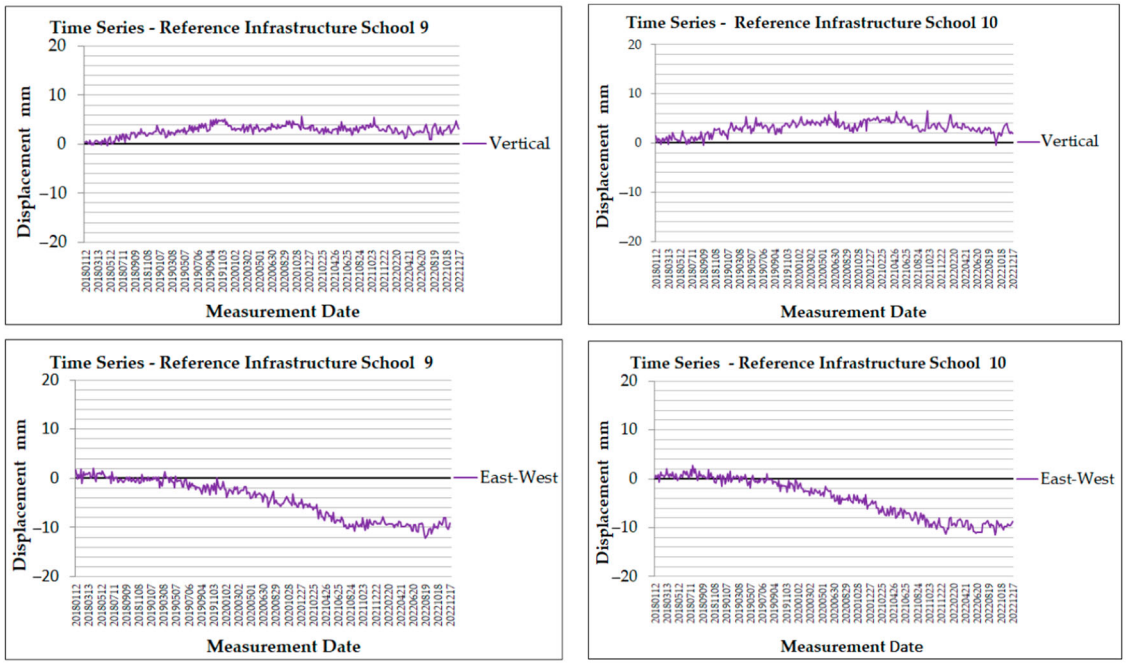

Figure 18. Times series for school infrastructures in area of Preveza (Schools 9–10).

The vertical displacement time series for MP near School 11 (Figure 19) shows a steady uplift from near the beginning of the dataset, with minimal fluctuations. The highest value of 5.6 mm is observed in August 2020. A few points indicate minor subsidence, with the lowest value of −1.2 mm being recorded in February 2018. The end of the dataset reveals a slight displacement of −0.6 mm. The east–west displacement presents a different trend. Until 2019, values vary around 0 with minimal variation. After October 2019, where the value is 0, a downward trend begins at a fast pace, reaching a minimum value of −12.1 mm

in February 2022 (2nd month). The westward movement continues at a steady rate until the end of the period, concluding at −10.2 mm.

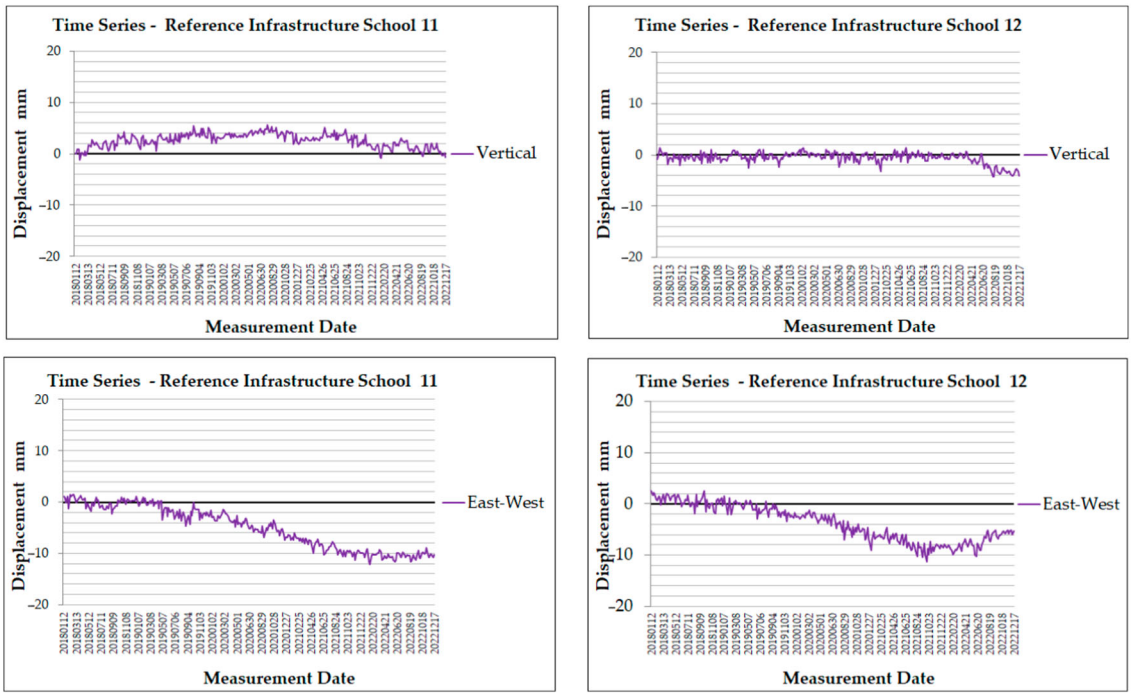

Figure 19. Times series for school infrastructures in area of Preveza (Schools 11–12).

The vertical displacement time series for School 12 (Figure 19) shows many low values during the dataset range around 0, from 1.4 mm to −4.3 mm. Only after June 2022, there is a small downward trend, with the lowest value of −4.3 mm in August 2022. The dataset concludes with a value of −4.1 mm. The east–west displacement time series reveals a clear downward trend, reaching −11.2 mm in October 2021. By the end of the period, the value of −5.3 mm indicates a slowing motion towards the west.

The vertical displacement time series of the MP for School 13 shows values around zero throughout the dataset, with slight fluctuations within a range of 1.5 mm to −3.1 mm. A minor subsidence is observed, with the lowest value of −3.1 mm observed in March 2020. The east–west displacement time series reveals a faster movement with frequent minor fluctuations. Almost from the beginning of the dataset, values are consistently negative showing a downward trend at a fast pace. The lowest value of −17.6 mm is observed in April 2022, highlighting the westward movement.

The vertical displacement time series for the MP near School 14 reveals a stable MP with minor fluctuations, with values remaining close to 0. The highest value is 3.3 mm, observed in June 2021, and the lowest is −2.7 mm at the end of the dataset. Most points indicate a slight uplift. The east–west displacement shows positive values at the beginning, indicating slight movement towards the east until August 2018. Until September 2019, values fluctuate around 0. After that point, the movement becomes clearly westward, reaching a minimum value of −11.1 mm in January 2022.

The time series that describes the motion of the MP for School 15 starts with values around 0. From May 2018, with a value of 1.2 mm, a slight uplift begins, following a stable course with mostly positive values. Throughout the dataset, values vary from 4.6 mm to −1.5 mm, concluding with a value of −0.6 mm. The east–west displacement time series shows an opposite trend to the vertical displacement. Although values are initially around 0, indicating slight eastward movement, a gradual westward movement appears after July 2019 (7th month). Values range from 3.1 mm to 12 mm throughout the dataset.

For School 16, the times series reveals values close to 0 at the beginning of the dataset until December 2018, where values show a slight upward trend, indicating a minor uplift until July 2020 (7th month). The lowest value of −3.5 mm is observed in August 2022, and the highest value of 4.2 mm occurs in both January 2020 and 2021. The dataset concludes with a displacement of −1 mm. The east–west displacement remains stable near zero at the beginning of the dataset. After May 2019, a downward trend with minor fluctuations appears, reaching a minimum of −11 mm in August 2018. The motion of the MP is westward, with a small recovery reaching −4.1 mm by the end of 2022.

For School 17, the time series (Figure 20) of vertical displacement shows values ranging from 3.5 mm to −2.6 mm throughout the dataset. Generally, the values are positive, indicating a minor uplift, except for a few points showing subsidence. From July 2022 until the end of the dataset, values remain negative, with the dataset ending at −1.4 mm. The east–west displacement time series shows that until the end of 2019, values have a range of 2.7 mm to −9.9 mm, with minor fluctuations and an overall downward trend. From the start of 2020, a steady downward trend appears, reaching a minimum of −9.9 mm in September 2021. After that point, values show a slight upward movement, not exceeding −4 mm, while remaining negative, indicating continued westward displacement.

3.3. Bridges of Ionia Odos

A total of four bridges along Ionia Odos were analyzed (Figure 21). All of them indicate a minor subsidence and fast westward movement. The vertical displacement time series for the MP of Bridge 1 shows values ranging from 0.9 mm to −12 mm (Figure 22), with values mostly negative during the study period. The east–west displacement reveals a westward movement. Initially, values fluctuate around 0; after 2019, a continuous downward trend appears, with values decreasing further.

The next time series depicts the displacement MP of Bridge 2. The vertical displacement values range from 5.4 mm to −20.6 mm, showing a gradual decline. The range in this dataset is bigger than that of the previous bridge. The lowest value of −20.6 mm is observed in November 2022, with the dataset concluding at −18.8 mm. The east–west displacement time series for Bridge 2 shows a range of values from 6 mm to −39.5 mm. Initially, values are around 0. There are troughs that consistently deepen over the time frame, indicating westward movement and reaching the lowest value of −39.5 mm in November 2022. Bridge 2, on the cumulative vertical, has a value of −18.8 mm and, in the east-west displacement cumulative, has a value of −38.8 mm (Figures 6 and 7).

The MP for Bridge 3 follows a similar trend to Bridge 1. Vertical displacement values range from 1.8 mm to −7.8 mm, indicating a slight subsidence. The east–west displacement shows a more pronounced downward trend, reflecting westward movement, with values ranging from 1.3 mm to −30.5 mm. Bridge 3, on the cumulative vertical, has a value of −7.5 mm and, in the east–west cumulative, has a value of −29.6 mm (Figures 6 and 7).

The MP for Bridge 4, the last one studied, shows vertical displacement values ranging from 6 mm to −8.5 mm. A minor subsidence is generally observed, with occasional instances of an uplift. The dataset ends with a value of −8.3 mm. The east–west displacement also indicates westward movement. In the beginning, there is a minor movement toward the east. After the end of 2018, there is a downward shift, with the lowest value of −28.2 mm in August 2022. Bridge 4, on the cumulative vertical, has a value of −8.3 mm and, in the east–west cumulative, has a value of −24.2 mm (Figures 6 and 7).

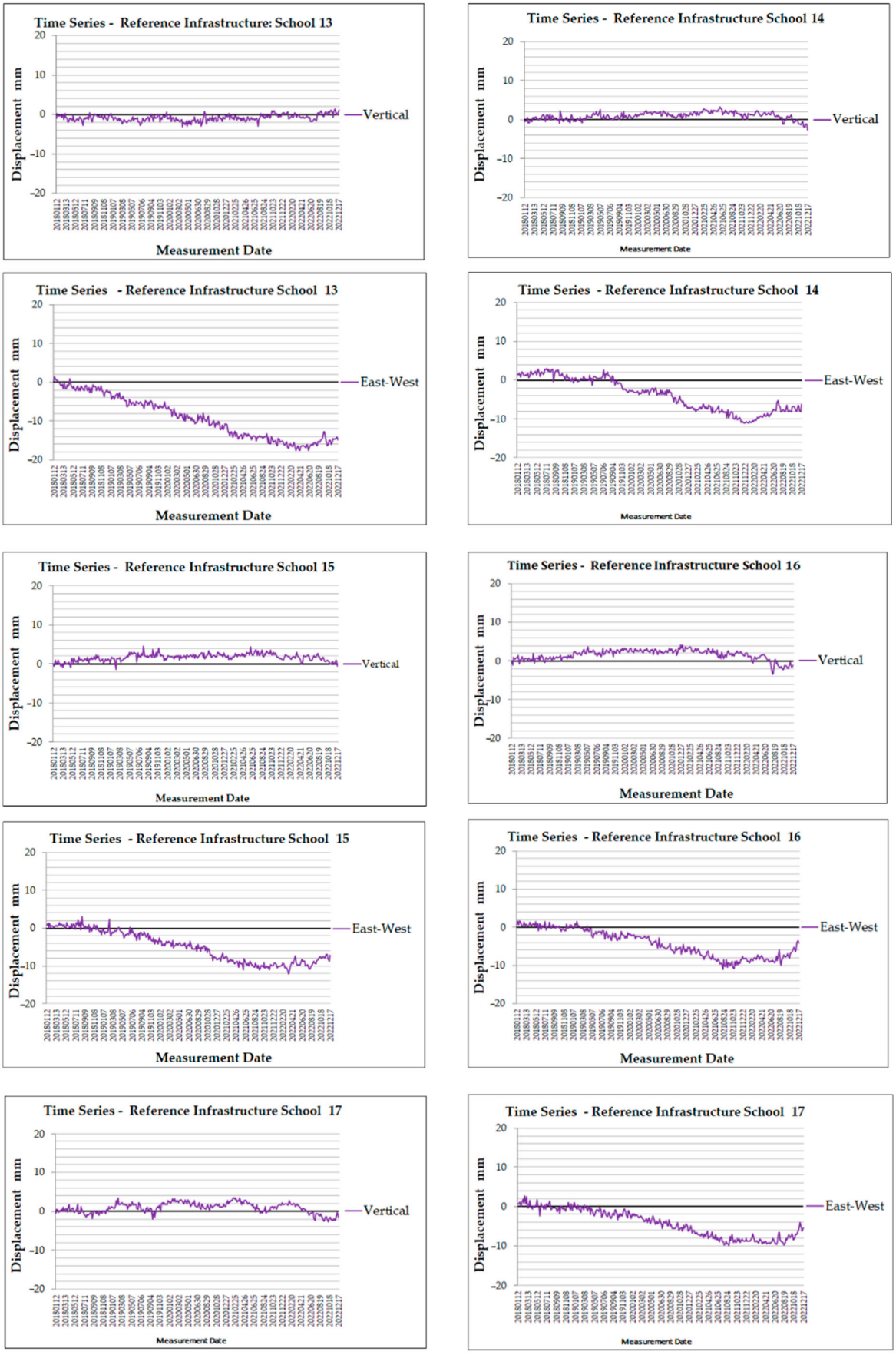

Figure 20. Times series for school infrastructures in area of Preveza (Schools 13–17).

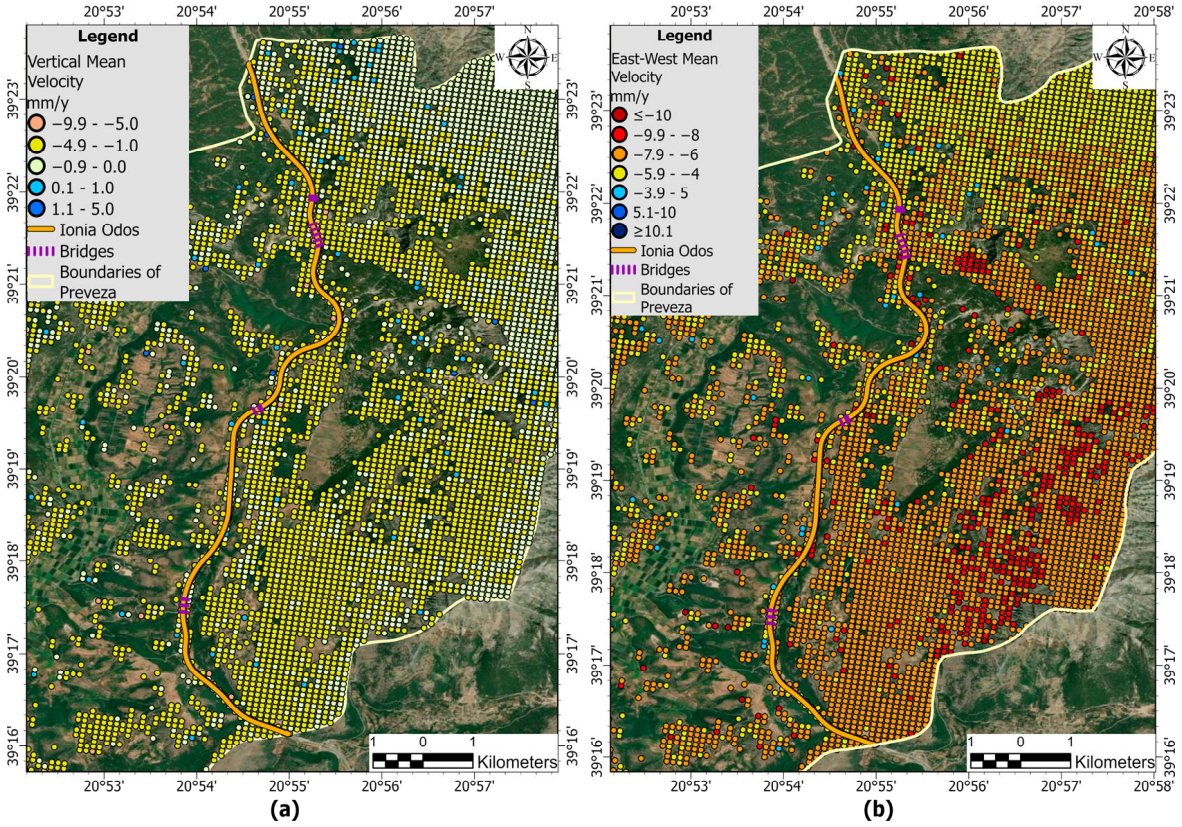

Figure 21. Bridges of Ionia Odos (vertical (**a**) and east–west (**b**) displacement).

Across all four bridges studied, a minor subsidence is generally observed in the mean velocity, although the cumulative values reveal more significant movement. Most bridges show a gradual downward trend, though none exhibit severe subsidence. Bridges 1, 3, and 4 show a smaller range of subsidence values, while Bridge 2 shows the greatest range. The east–west displacement is more significant than the vertical displacement across all bridges. Most bridges start with values around zero, but Bridge 2 shows the biggest range of values in this direction as well.

3.4. Dam

The last infrastructure monitored is the dam of the Louros river. The vertical displacement time series of the MP reveals an unstable trend (Figure 23). Values fluctuate rapidly, with sharp changes at multiple points, ranging from 4.5 mm to −11.2 mm throughout the dataset. Overall, the data indicates subsidence, with the lowest value of −11.2 mm recorded at the end of the dataset. The east–west displacement shows a steady downward trend, revealing westward movement. At the beginning of the dataset, until the 6th month of 2018, values fluctuate around 0. After that point, values remain negative. In the dataset, values range from 2.4 mm to −39.6 mm.

The MP for the dam we are monitoring shows a cumulative vertical displacement of −11.2 mm, which is indicative of subsidence. The cumulative displacement for the east–west direction at the dam is −25.7 mm, indicating considerable horizontal movement towards the west. (Figures 6 and 7)

Additionally, a buffer zone was created around the critical infrastructures (Figures 24 and 25) to identify the monitoring points located near the area of interest. Every buffer zone includes at least four MPs. This approach ensures a focused analysis of the spatial distribution in the immediate vicinity of the infrastructures analyzed. The time-series analysis for the selected MPs within the buffer zone represents all the patterns in the MPs

across the buffered area without diversities. This indicates that a single representative MP is sufficient to depict the deformation trends for the zone, as the data are spatially uniform within this region.

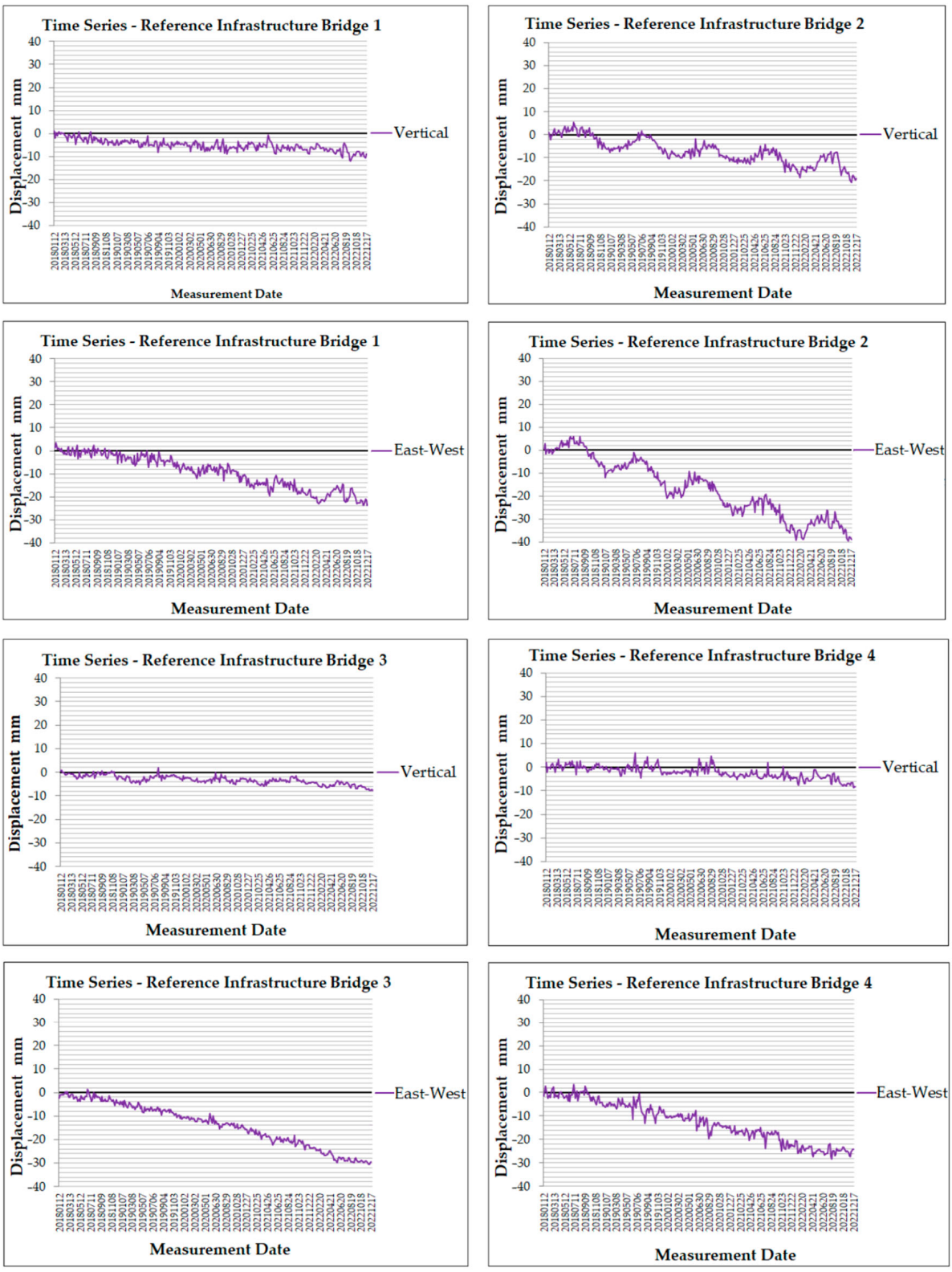

Figure 22. Times series for referenced infrastructures bridges of Ionia Odos.

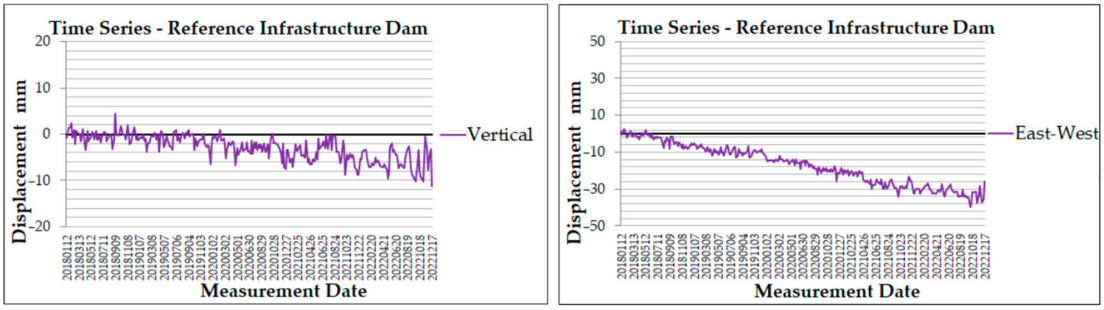

Figure 23. Time series for referenced infrastructure: dam.

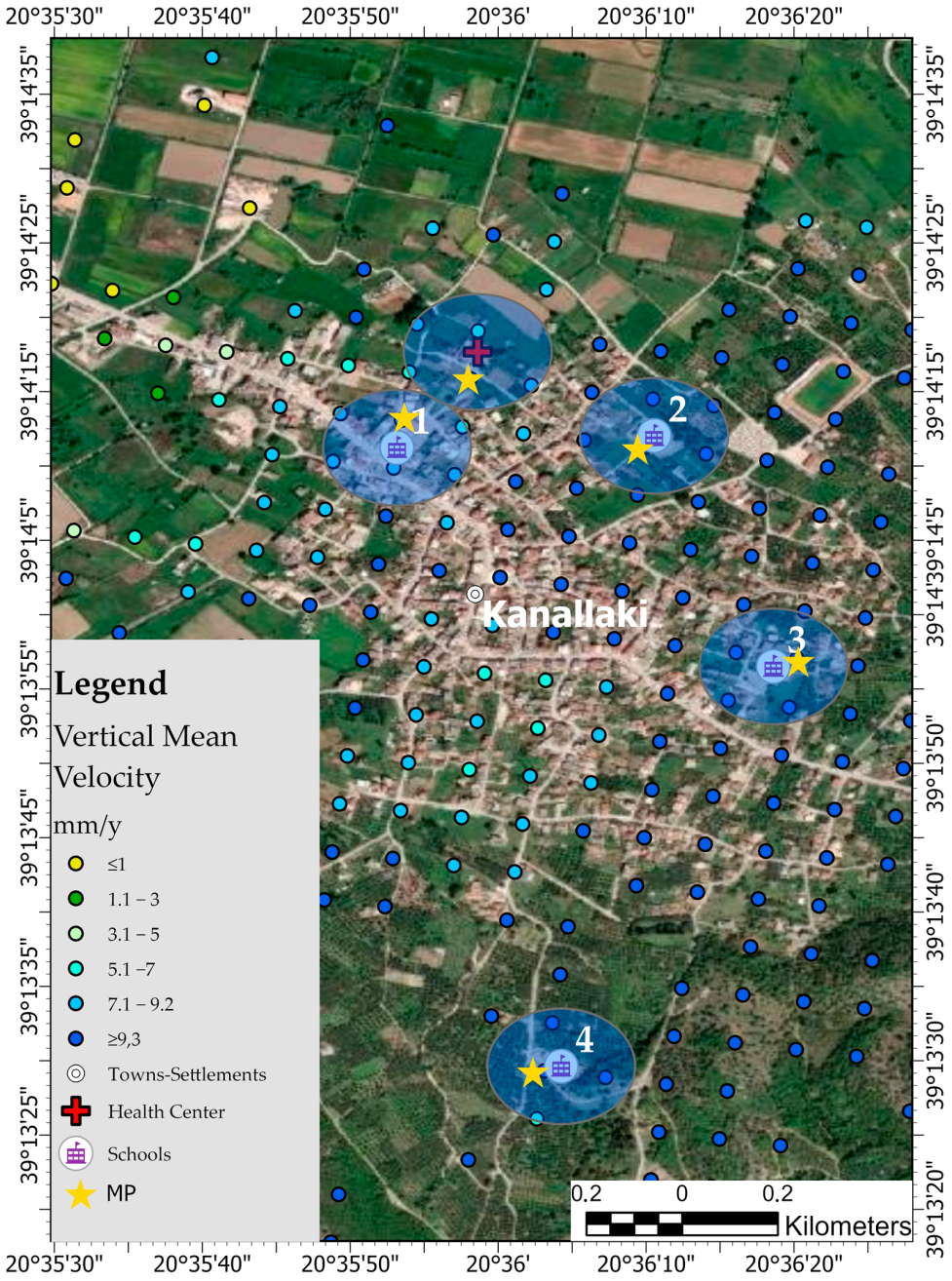

Figure 24. Spatial distribution of detected monitoring points (MPs) near the critical infrastructures in the study area of Kanallaki. The blue-shaded buffer zones represent areas surrounding the critical infrastructures, each containing at least four MPs.

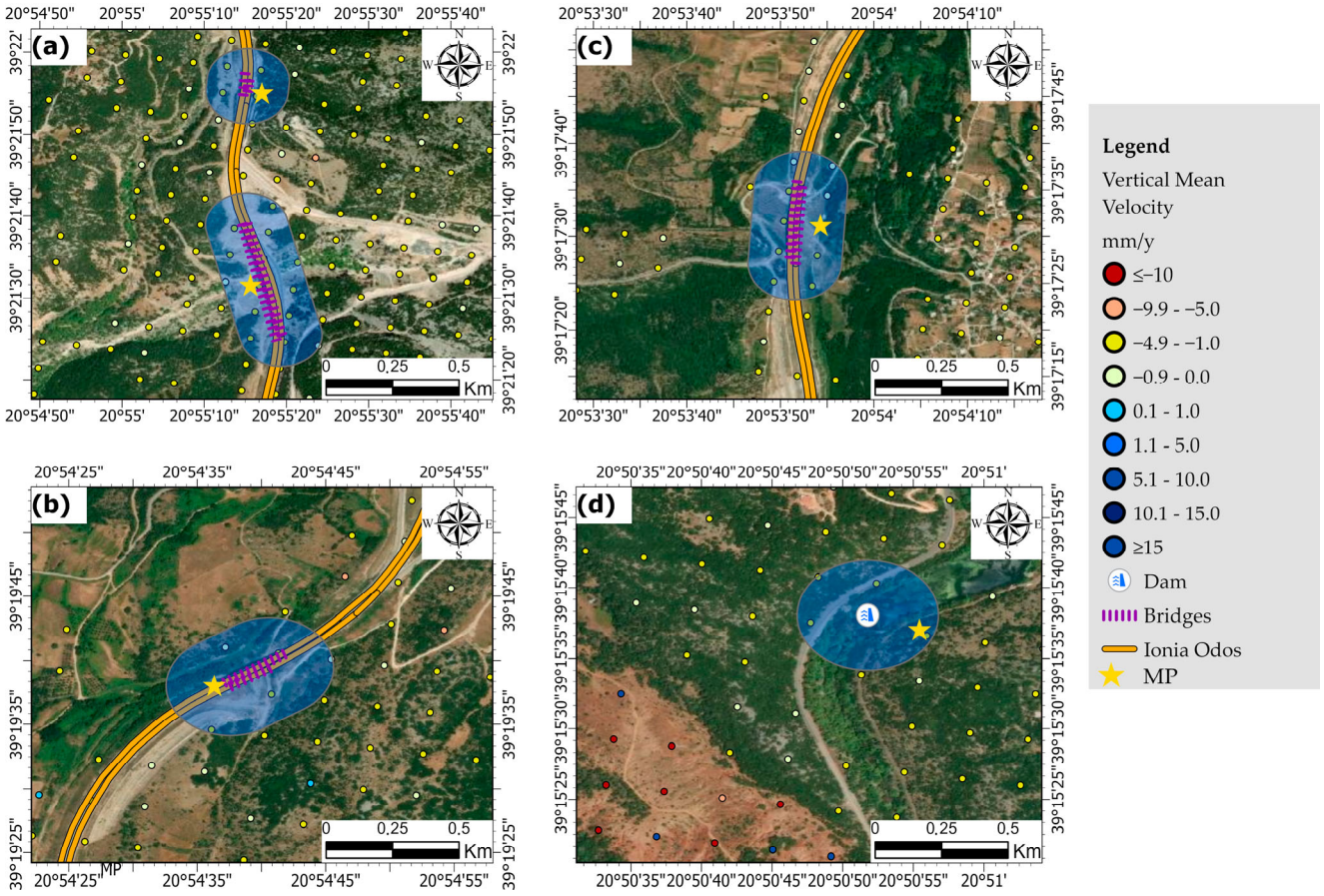

Figure 25. Spatial distribution of detected monitoring points (MPs) near the critical infrastructures in the study area. From north to south: Panel (**a**) depicts Bridges 1 and 2, Panel (**b**) depicts Bridge 3, Panel (**c**) depicts Bridge 4, and Panel (**d**) depicts the dam. The blue-shaded buffer zones represent areas surrounding the infrastructures, each containing at least four MPs.

4. Discussion

By integrating geospatial data concerning critical infrastructures with data from the EGMS, this study effectively assessed ground vulnerability in the Regional Unit of Preveza. The analysis provides a comprehensive understanding of the spatial distribution and magnitude of ground motion in the area, highlighting key areas of concern. In most parts of Preveza, the vertical displacement reveals values between 0 mm/y and −4.9 mm/y, indicating a general trend of slight subsidence. Coastal areas reveal values ranging from −4.9 mm/y to 5 mm/y. Notably, the area near Kanallaki reveals an upward trend in the vertical displacement, with values ranging from 0.1 mm/y to 16 mm/y, represented by blue, dark blue, and green dots. This trend in Kanallaki deviates significantly from the general pattern observed in the rest of the Regional Unit (Figure 3). This anomaly in Kanallaki coincides with geological formations primarily composed of Plio-Quaternary deposits, as illustrated in the geological map (Figure 8), which are more susceptible to ground deformation and subsidence.

A distinct pattern emerges in the displacement time series of the health center and the four schools in the settlement of Kanallaki. The data reveal an initial subsidence phase, followed by a period of recovery and finally a notable sudden uplift. According to the data, in March 2020, values in these locations suddenly increased, reaching 26.7 mm at the MP near School 1, 40.2 mm at School 2, 30.4 mm near School 3, 21.9 mm for the MP near School 4, and 26.8 mm at the MP near the health center. This consistent pattern across all five infrastructures of Kanallaki is in close agreement with the findings of Svigkas et al. [47],

who documented a significant movement of the ground towards the satellite of approximately 6 cm by utilizing DinSAR technology. Also, the findings of Lekkas et al. [30] and Valkaniotis et al. [31], who documented a significant uplift associated with the earthquake in the western region of Epirus on 21 March 2020 (Figure 2), are similar to the results of this study. Specifically, the maximum vertical displacement at 4 cm was reported by Valkaniotis [31]. The timing and magnitude of the observed uplift in the dataset corroborate these findings, particularly the maximum vertical displacement of 6 cm reported in their study. Polcari et al. [48], also utilizing Sentinel-1 InSAR data, revealed an approximate LoS displacement of 3 cm in the area of Kanallaki. There is no significant distinction between our results and the conclusions of any prior research, and there is close agreement between the results.

In contrast, the dam and the four bridges analyzed in this study are located on the eastern side of the Preveza region, where vertical displacement is more moderate compared to the ground motion in Kanallaki. This more stable pattern suggests that the eastern area was less affected by the 2020 earthquake. This observation is supported by the consistent, steady patterns seen across other parts of the region, indicating that ground stability remains high outside the Kanallaki area.

The mean east–west velocity in the area of Preveza ranges from 22.5 mm/y to −37.7 mm/y (Figure 5). Coastal settlements like Preveza and Parga reveal a moderate movement towards the west, as shown by green dots (−4.9 mm/y to 0 mm/y) (Figure 5). Northeastern areas near Filippiada and west of Kanallaki reveal a faster westward movement, represented by yellow dots (Figure 5) (values between −9.9 mm/y to −5 mm/y). Isolated points south and southeast of Kanallaki show an eastward motion, with values around 10 mm/y. North of Thesprotiko, several points show intense westward movement, indicated by red and dark red dots, which represent the fastest motion rates (exceeding −15 mm/y). The east–west displacement of the four bridges and the dam also confirms a rapid westward motion, reflecting a more pronounced lateral movement than the vertical displacement in these infrastructures.

The infrastructures in the area of Preveza, as a whole, show a moderate vertical and east–west displacement, implying a minimal hazard risk at the time of the study; this suggests a low potential risk from ground motion, with southern Preveza appearing particularly stable when compared to the Kanallaki area. The stability of measurement points in eastern Preveza, with few sudden changes or deviations in the vertical mean velocity (Figure 13), supports the observation that this region is less vulnerable to seismic events than areas closer to Kanallaki. Notable exceptions include the port of Preveza, where slight subsidence is observed, likely driven by anthropogenic influences, and Schools 1, 2, 3, and 16, which show a higher tendency for subsidence compared to other infrastructures.

Cumulative displacement maps (Figures 6 and 7) highlight two main areas with notable displacement variations. The first is the settlement of Kanallaki, where, in addition to the sudden uplift observed in March 2020, reflected in the time series of nearby infrastructures, cumulative data reveal heightened vulnerability around critical infrastructures. Significant cumulative displacement values have been recorded for most of Kanallaki's key infrastructures, indicating a high degree of vulnerability, particularly in terms of vertical displacement. It is worth emphasizing that the 2020 earthquake not only triggered an abrupt uplift but also that the cumulative displacement data reinforces this observation, underscoring the area's susceptibility to ground deformation.

The second area exhibiting significant displacement is located on the eastern side of the region, where the dam and bridges are situated. This area shows cumulative east–west displacement values reaching up to −42.4 mm and vertical displacement values up to −23.3 mm. The proximity of major faults in this zone further amplifies its vulnerability.

The dam analyzed in this study is located near an area of pronounced subsidence. The nearby MPs, particularly those marked in red and orange on the map (Figure 4), display significant vertical displacement, underscoring the dam's proximity to zones of ground instability. This raises concerns regarding potential impacts on the structural stability of the dam. The MP associated with the dam exhibits a cumulative vertical displacement of −11.2 mm, indicating ongoing subsidence. This value highlights the dam's proximity to a region characterized by significant ground movement, as reflected in the vertical mean velocity data. Additionally, the cumulative east–west displacement at the dam is recorded at −25.7 mm, indicating considerable horizontal movement towards the west.

Among all the bridges studied along Ionia Odos, three exhibit significant cumulative displacement values. As noted by Gao et al. [2], subsidence in areas with infrastructure embankments is a common phenomenon in deformation studies, often attributed to heavy traffic loads. Additionally, the presence and magnitude of earthquakes (Figure 2) play a crucial role in determining infrastructure vulnerability. Areas that experience frequent seismic activity or high-magnitude events are more susceptible to ground motion, structural damage, and potential ground failure, further increasing the risk to critical infrastructures.

The Kanallaki region is highly seismically active, experiencing regular earthquakes of notable magnitude. This increased seismic activity makes the area more vulnerable compared to the rest of the region, particularly in terms of the resilience of infrastructure and settlements. Higher cumulative displacements are frequently observed in infrastructures located near fault lines (Figure 2). Proximity to seismic faults heightens the risk of ground deformation, which can significantly impact the stability and functionality of nearby infrastructures, including bridges, schools, medical facilities, and dams.

The findings of this study align with the research of Cigna et al. [49], whose InSAR- and PSI-based deformation maps demonstrate spatial correlations with major fault lines. Tectonic activity along faults can alter the structure of adjacent layers, resulting in uneven ground subsidence on either side of the fault. Similarly, Yang et al. [50] observed coseismic surface deformation around seismic faults in his research. These studies collectively underscore that areas in proximity to fault lines are inherently more vulnerable to ground deformation.

Additionally, the uniformity of the motion data across the buffer zones (Figures 24 and 25) suggests that redundancy in monitoring points and the generation of time series is minimal. This enhances the efficiency of the analysis by reducing the need for multiple MPs while still accurately reflecting the deformation trends in the area. This observation aligns with the findings of Wassie et al. [51], who indicated that measurement points within the buffer zone are stable, and their scores reflect the reliability of measurements.

The resolution of EGMS products enables the detection of deformations in the immediate surroundings of bridges and other infrastructures. However, this resolution may present limitations in capturing highly localized displacements in specific bridge elements. Despite these limitations, deformations detected in the surrounding terrain serve as key indicators of potential structural impacts. Furthermore, for the long-term monitoring of such deformations, Sentinel-1's revisit period of 6–12 days is generally sufficient to identify significant changes in infrastructure stability.

Overall, the Regional Unit of Preveza demonstrates a moderate pattern of displacement, with the exception of the area of Kanallaki, which presents an anomaly in terms of ground motion. This unique pattern needs further investigation to understand its impact on ground vulnerability and infrastructure resilience in the Preveza region. The 2020 earthquake serves as a timely reminder of the region's seismic susceptibility. The continued monitoring of this area will be essential for assessing the potential long-term effects of

seismic activity on the stability of critical infrastructures, given historical data indicating that moderate to large earthquakes are likely to occur periodically.

5. Conclusions

Using geospatial data from critical infrastructures and the EGMS, this study provided valuable insights into the distribution and magnitude of ground motion in the Preveza Regional Unit. The findings underscore the importance of focused monitoring in two main areas. Firstly, the area of Kanallaki exhibits significant vertical displacement and cumulative motion, likely linked to the 2020 earthquake. Critical infrastructures, such as schools and the health center, recorded cumulative vertical displacements of up to 33.6 mm and east–west displacements of up to −18.7 mm. This trend highlights high ground vulnerability, with potential implications for structural stability.

The second area of concern is where the dam and the bridges of Ionia Odos are located. The dam and the four nearby bridges show considerable accumulated vertical displacement, reaching up to −18.8 mm, and even more pronounced cumulative east–west displacement, with values up to −38.8 mm. Proximity to major fault lines further amplifies the vulnerability of these infrastructures, underscoring the need for ongoing structural assessments.

Additionally, the port of Preveza and Schools 1, 2, 3, and 16 are located in an area experiencing moderate vertical displacement. As the port plays a crucial role in the region's economy, continued monitoring is vital to prevent disruptions and ensure safety. The 2020 earthquake induced significant ground uplift, particularly in Kanallaki, resulting in high vertical displacements at several measurement points. These findings are consistent with previous research, reaffirming the seismic susceptibility of the region. Areas near fault lines experience pronounced ground deformation, reinforcing the link between tectonic activity and infrastructure instability. Continuous updates and analyses of ground deformation data will be crucial for developing mitigation strategies and enhancing the resilience of critical infrastructures across the region.

Author Contributions: Conceptualization, I.C.-M. and I.P.; methodology, E.B.; software, E.B. and A.K.; validation, E.B., I.C.-M. and A.K.; formal analysis, E.B.; investigation, E.B. and I.C.-M.; resources, E.B. and A.K.; data curation, E.B., H.K. and E.L.; writing—original draft preparation, E.B. and I.C.-M.; writing—review and editing, E.B., I.C.-M., H.K., A.K., E.L. and I.P.; visualization, E.B. and A.K.; supervision, I.C.-M. and I.P.; project administration, I.P.; funding acquisition, I.P. All authors have read and agreed to the published version of the manuscript.

Funding: No external funding was acquired for this work.

Data Availability Statement: The EGMS products can be downloaded from https://egms.land.copernicus.eu/ (accessed on 15 June 2024).

Acknowledgments: The EGMS data were accessed through the European Ground Motion Service https://egms.land.copernicus.eu, accessed on June 2024, and processed and visualized by utilizing ArcPro Software v. 3.

Conflicts of Interest: The authors declare no conflicts of interest.

Appendix A

Table A1. Vertical and east–west displacement of point-like infrastructures of the area of Kanallaki (schools, health center); Pid is a unique identifier assigned to each MP.

Infrastructure	Lat.	Long.	V. Displ. (mm/y)	E-W Displ. (mm/y)	Pid
Health Center	39.2381597	20.5995932	6.9	−4.5	10Mf5BYBTi
School 1	39.2364503	20.5981019	7.1	−3.2	10Mf0UswHd
School 2	39.2366767	20.6028675	12	−3.9	10Mf0UswHh
School 3	39.2324173	20.6051721	11.7	−4.1	10MehkDxVU
School 4	39.2249225	20.6011731	11	−4.6	10Me1YEkkr

Table A2. Vertical and east–west displacement of point-like infrastructures of area of Preveza (hospital, health center, schools); Pid is a unique identifier assigned to each MP.

Infrastructure	Lat.	Long.	V. Displ. (mm/y)	E-W Displ. (mm/y)	Pid
Hospital	38.9655006	20.7536955	−0.2	−2.3	10MJuVHZ2P
Health Center	38.9632509	20.7503009	−0.1	−2.3	10MJgRHpSA
School 1	38.9586934	20.7532018	−0.1	−2.7	10MJNgcqfy
School 2	38.9564813	20.7520079	−0.4	−2.5	10MJ9cd75l
School 3	38.9533716	20.7508451	−0.2	−2.5	10MIvYdNVY
School4	38.9667946	20.7456386	−0.2	−2.5	10MJzBwoEM
School 5	38.9538455	20.7451430	−0.3	−2.7	10MIqry8JP
School 6	38.9602587	20.7453070	0.1	−2.5	10MJSNI5rv
School 7	38.9790451	20.7727355	−0.4	−2.9	10MLCCajLj
School 8	38.9791537	20.7443548	0	−3.2	10MKy8azl9
School 9	38.9472789	20.7371700	0.3	−2.7	10MIFMeAkn
School 10	38.9581290	20.7393146	0.4	−2.8	10MJEJIMHe
School 11	38.9550177	20.7404788	−0.2	−2.8	10MIvYdNVP
School 12	38.9690838	20.7513878	−0.3	−2.3	10MKDFwXoc
School 13	39.0002839	20.7092027	0.2	−3.8	10MMPDEeRq
School 14	38.9762020	20.7437461	0.1	−2.8	10MKk4bGAx
School 15	38.9727127	20.7478706	0.2	−2.7	10MKRJwHOl
School 16	38.9539741	20.7507981	−0.1	−2.3	10MJ0FIchc
School 17	38.9626656	20.7470600	0	−2.3	10MJbkcaG3

Table A3. Vertical and east–west displacement of linear infrastructures (bridges of Ionia Odos, from north to south); Pid is a unique identifier assigned to each MP.

Infrastructure	Lat.	Long.	V. Displ. (mm/y)	E-W Displ. (mm/y)	Pid
Bridge 1	39.3653666	20.9207942	−1.3	−5	10MscMd3NQ
Bridge 2	39.3600797	20.9211537	−3.4	−8.5	10Ms5XyL0z
Bridge 3	39.3275666	20.9109317	−1.1	−6.3	10MpMm1W0a
Bridge 4	39.2922036	20.8976423	−1.4	−5.8	10MmLFPiDu

Table A4. Vertical and east–west displacement of dam; Pid is a unique identifier assigned to each MP.

Infrastructure	Lat.	Long.	V. Displ. (mm/y)	E-W Displ. (mm/y)	Pid
Dam	39.2605736	20.8477167	−1.5	−7.4	10MjF28fEf

Appendix B

Table A5. Vertical and east–west cumulative values of point-like infrastructures of the area of Kanallaki (schools, health center); Pid is a unique identifier assigned to each MP.

Infrastructure	Lat.	Long.	V. Cumulative (mm)	E-W Cumulative (mm)	Pid
Health Center	39.2381597	20.5995932	14.1	−18.7	10Mf5BYBTi
School 1	39.2364503	20.5981019	16.1	−13.5	10Mf0UswHd
School 2	39.2366767	20.6028675	33.6	−15.1	10Mf0UswHh
School 3	39.2324173	20.6051721	30.9	−13.7	10MehkDxVU
School 4	39.2249225	20.6011731	33	−17.9	10Me1YEkkr

Table A6. Vertical and east–west cumulative values of point-like infrastructures of area of Preveza (hospital, health center, schools); Pid is a unique identifier assigned to each MP.

Infrastructure	Lat.	Long.	V. Cumulative (mm)	E-W Cumulative. (mm)	Pid
Hospital	38.9655006	20.7536955	−2.1	−5	10MJuVHZ2P
Health Center	38.9632509	20.7503009	−1.3	−5.5	10MJgRHpSA
School 1	38.9586934	20.7532018	−0.5	−7.5	10MJNgcqfy
School 2	38.9564813	20.7520079	−1.6	−6.4	10MJ9cd75l
School 3	38.9533716	20.7508451	−1.9	−5.9	10MIvYdNVY
School 4	38.9667946	20.7456386	−2.8	−6.8	10MJzBwoEM
School 5	38.9538455	20.7451430	−2.1	−9.7	10MIqry8JP
School 6	38.9602587	20.7453070	−1.5	−5.7	10MJSNI5rv
School 7	38.9790451	20.7727355	−5.9	−9.7	10MLCCajLj
School 8	38.9791537	20.7443548	−3.7	−8.4	10MKy8azl9
School 9	38.9472789	20.7371700	3.1	−9.1	10MIFMeAkn
School 10	38.9581290	20.7393146	2	−8.8	10MJEJIMHe
School 11	38.9550177	20.7404788	−0.6	−10.2	10MIvYdNVP
School 12	38.9690838	20.7513878	−4.1	−5.3	10MKDFwXoc
School 13	39.0002839	20.7092027	1.1	−14.8	10MMPDEeRq
School 14	38.9762020	20.7437461	−2.7	−6.2	10MKk4bGAx
School 15	38.9727127	20.7478706	−0.6	−7.2	10MKRJwHOl
School 16	38.9539741	20.7507981	−1	−4.1	10MJ0FIchc
School 17	38.9626656	20.7470600	−1.4	−5.4	10MJbkcaG3

Table A7. Vertical and east–west cumulative values of linear infrastructures (bridges of Ionia Odos, from north to south); Pid is a unique identifier assigned to each MP.

Infrastructure	Lat.	Long.	V. Cumulative (mm)	E-W Cumulative. (mm)	Pid
Bridge 1	39.3653666	20.9207942	−10.8	−23.9	10MscMd3NQ
Bridge 2	39.3600797	20.9211537	−18.8	−38.8	10Ms5XyL0z
Bridge 3	39.3275666	20.9109317	−7.5	−29.6	10MpMm1W0a
Bridge 4	39.2922036	20.8976423	−8.3	−24.2	10MmLFPiDu

Table A8. Vertical and east–west cumulative displacement of dam; Pid is a unique identifier assigned to each MP.

Infrastructure	Lat.	Long.	V. Cumulative (mm)	E-W Cumulative (mm)	Pid
Dam	39.2605736	20.8477167	−11.2	−25.7	10MjF28fEf

References

1. European Union. Available online: https://eur-lex.europa.eu (accessed on 20 June 2024).
2. Gao, Q.; Crosetto, M.; Monserrat, O.; Palama, R.; Barra, A. Infrastructure Monitoring Using the Interferometric Synthetic Aperture Radar (INSAR) Technique. *Int. Arch. Photogramm. Remote Sens. Spat. Inf. Sci.* **2022**, *43*, 271–276. [CrossRef]
3. EGMS Task Force. 2017. Available online: https://land.copernicus.eu/user-corner/technical-library/egms-white-paper (accessed on 28 July 2024).
4. Crosetto, M.; Solari, L.; Balasis-Levinsen, J.; Casagli, N.; Frei, M.; Oyen, A.; Moldestad, D.A. Ground deformation monitoring at continental scale: The European Ground Motion Service. *Int. Arch. Photogramm. Remote Sens. Spat. Inf. Sci.* **2020**, *43*, 293–298. [CrossRef]
5. Costantini, M.; Minati, F.; Trillo, F.; Ferretti, A.; Novali, F.; Passera, E.; Dehls, J.; Larsen, Y.; Marinkovic, P.; Eineder, M.; et al. European Ground Motion Service. In Proceedings of the International Geoscience and Remote Sensing Symposium (IGARSS), Brussels, Belgium, 11–16 July 2021; pp. 3293–3296. [CrossRef]
6. European Environment Agency. Available online: https://www.eea.europa.eu/en/datahub (accessed on 5 September 2024).
7. Kotzerke, P.; Siegmund, R.; Langenwalter, J.; Andersen, H.S. *End-to-End Implementation and Operation of the European Ground Motion Service (EGMS) Product User Manual EGMS SC1 ORIGINAL Consortium Product User Manual (D4-PUM) Document Control Information Settings Value Document Title: Product User Manual Project Title: EGMS-SC1*; European Environment Agency: Copenhagen, Denmark, 2022.
8. Upadhyay, P.; Czerkawski, M.; Davison, C.; Cardona, J.; Macdonald, M.; Andonovic, I.; Michie, C.; Atkinson, R.; Papadopoulou, N.; Nikas, K.; et al. A Flexible Multi-Temporal and Multi-Modal Framework for Sentinel-1 and Sentinel-2 Analysis Ready Data. *Remote Sens.* **2022**, *14*, 1120. [CrossRef]
9. Dang, B. Comparison of Polarization Models in SAR technology for Water Body Extraction. KTH Royal Institute of Technology, 2024. Available online: https://kth.diva-portal.org/smash/get/diva2:1901548/FULLTEXT01.pdf (accessed on 10 November 2024).
10. Massonnet, D.; Feigl, K.L. Radar interferometry and its application to changes in the Earth's surface. *Rev. Geophys.* **1998**, *36*, 441–500. [CrossRef]
11. Bekaert, D.P.S.; Handwerger, A.L.; Agram, O.; Kirschbaum, D.B. InSAR-based detection method for mapping and monitoring slow-moving landslides in remote regions with steep and mountainous terrain: An application to Nepal. *Remote Sens. Environ.* **2020**, *249*, 111983. [CrossRef]
12. Tizzani, P.; Fernández, J.; Vitale, A.; Escayo, J.; Barone, A.; Castaldo, R.; Pepe, S.; De Novellis, V.; Solaro, G.; Pepe, A.; et al. 4D imaging of the volcano feeding system beneath the urban area of the Campi Flegrei caldera. *Remote Sens. Environ.* **2024**, *315*, 114480. [CrossRef]
13. Lekkas, E.; Meletlidis, S.; Kyriakopoulos, K.; Manousaki, M.; Mavroulis, S.; Kostaki, E.; Michailidis, A.; Gogou, M.; Mavrouli, M.; Castro-Melgar, I.; et al. The 2021 Cumbre Vieja volcano eruption in La Palma (Canary Islands). *Newsl. Environ. Disaster Cris. Manag. Strateg.* **2021**, *26*, 167. [CrossRef]
14. Castro-Melgar, I.; Gatsios, T.; Prudencio, J.; Ibanez, J.M.; Lekkas, E.; Parcharidis, I. Volcano Monitoring: Using SAR Interferometry for the Pre-Unrest of La Palma and the Post-Unrest of Santorini. In *Remote Sensing for Geophysicists*, 1st ed.; Gupta, M., Ed.; CRC Press Taylor & Francis Group: Boca Raton, FL, USA, 2025; p. 526. ISBN 978-1-032-77892-1.
15. Brozzetti, F.; Mondini, A.C.; Pauselli, C.; Mancinelli, P.; Cirillo, D.; Guzzetti, F.; Lavecchia, G. Mainshock Anticipated by Intra-Sequence Ground Deformations: Insights from Multiscale Field and SAR Interferometric Measurements. *Geosciences* **2020**, *10*, 186. [CrossRef]
16. He, L.J.; Feng, G.C.; Xu, W.B.; Wang, Y.D.; Xiong, Z.Q.; Gao, H.; Liu, X.G. Coseismic Kinematics of the 2023 Kahramanmaras, Turkey Earthquake Sequence from InSAR and Optical Data. *Geophys. Res. Lett.* **2023**, *50*, e2023GL104693. [CrossRef]
17. Yazbeck, J.; Rundle, J.B. A Fusion of Geothermal and InSAR Data with Machine Learning for Enhanced Deformation Forecasting at the Geysers. *Land* **2023**, *12*, 1977. [CrossRef]
18. Ghorbani, Z.; Khosravi, A.; Maghsoudi, Y.; Mojtahedi, F.F.; Javadnia, E.; Nazari, A. Use of InSAR data for measuring land subsidence induced by groundwater withdrawal and climate change in Ardabil Plain. *Iran. Sci. Rep.* **2022**, *12*, 13998. [CrossRef] [PubMed]
19. Biggs, J.; Wright, T.J. How satellite InSAR has grown from opportunistic science to routine monitoring over the last decade. *Nat. Commun.* **2020**, *11*, 3863. [CrossRef] [PubMed]
20. Kalavrezou, I.-E.; Castro-Melgar, I.; Nika, D.; Gatsios, T.; Lalechos, S.; Parcharidis, I. Application of Time Series INSAR (SBAS) Method Using Sentinel-1 for Monitoring Ground Deformation of the Aegina Island (Western Edge of Hellenic Volcanic Arc). *Land* **2024**, *13*, 485. [CrossRef]
21. Parcharidis, I.; Foumelis, M. On the assessment of Co-seismic InSAR images of different time span associated to Athens (Greece) 1999 Earthquake. In Proceedings of the International Geoscience and Remote Sensing Symposium (IGARSS), Seoul, Republic of Korea, 29 July 2005; pp. 5251–5254. [CrossRef]

22. Crosetto, M.; Solari, L.; Balasis-Levinsen, J.; Bateson, L.; Casagli, N.; Comerci, V.; Frei, M.; Guerrieri, L.; Mroz, M.; Moldestad, D.A.; et al. Ground Motion Examples from the European Ground Motion Service. In Proceedings of the International Geoscience and Remote Sensing Symposium (IGARSS), Kuala Lumpur, Malaysia, 17–22 July 2022; pp. 5109–5112. [CrossRef]
23. Gatsios, T.; Cigna, F.; Tapete, D.; Sakkas, V.; Pavlou, K.; Parcharidis, I. Copernicus sentinel-1 MT-InSAR, GNSS and seismic monitoring of deformation patterns and trends at the Methana volcano, Greece. *Appl. Sci.* **2020**, *10*, 6445. [CrossRef]
24. Rocca, F.; Rucci, A.; Ferretti, A.; Bohane, A. Advanced InSAR interferometry for reservoir monitoring. *First Break.* **2013**, *31*, 68075. [CrossRef]
25. Ferretti, A.; Passera, E.; Capes, R.; Steen Andersen, H.; Solari, L. *End-to-End Implementation and Operation of the European Ground Motion Service (EGMS): Algorithm Theoretical Basis Document*; European Environment Agency: Copenhagen, Denmark, 2021.
26. Citypopulation. Available online: https://www.citypopulation.de (accessed on 20 August 2024).
27. King, G.C.P.; Tselentis, A.; Gomberg, J.; Molnar, P.; Roecker, S.W.; Sinvhal, H.; Soufleris, C.; Stock, J.M. Microearthquake seismicity and active tectonics of northwestern Greece. *Earth Planet. Sci. Lett.* **1983**, *66*, 279–288. [CrossRef]
28. Ntokos, D. Formulation of the conceptual model for the tectonic geomorphological evolution of an area: Five main rivers of Greece as a case study. *Catena* **2018**, *167*, 60–77. [CrossRef]
29. Ntokos, D. Neotectonic study of northwestern Greece. *J. Maps.* **2018**, *14*, 178–188. [CrossRef]
30. Lekkas, E.; Mavroulis, S.; Carydis, P.; Skourtsos, E.; Kaviris, G.; Paschos, P.; Ganas, A.; Kazantzidou-Firtinidou, D.; Parcharidis, I.; Gatsios, T.; et al. The 21 March 2020 Mw 5.7 Epirus (Greece) Earthquake. *Newsl. Environ. Disaster Cris. Manag. Strateg.* **2020**, *17*, 75. [CrossRef]
31. Valkaniotis, S.; Briole, P.; Ganas, A.; Elias, P.; Kapetanidis, V.; Tsironi, V.; Fokaefs, A.; Partheniou, H.; Paschos, P. The Mw = 5.6 Kanallaki Earthquake of 21 March 2020 in West Epirus, Greece: Reverse Fault Model from InSAR Data and Seismotectonic Implications for Apulia-Eurasia Collision. *Geosciences* **2020**, *10*, 454. [CrossRef]
32. Papazachos, B.; Papazachou, C. *The Earthquakes of Greece*; Editions Ziti: Thessaloniki, Greece, 1997.
33. Ganas, A.; Oikonomou, I.A.; Tsimi, C. NOA faults: A digital database for active faults in Greece. *Bull. Geol. Soc. Greece* **2013**, *47*, 518–530. [CrossRef]
34. Tsapanos, T.M. Seismicity and Seismic Hazard Assessment in Greece. In *Earthquake Monitoring and Seismic Hazard Mitigation in Balkan Countries*; Springer: Dordrecht, The Netherlands, 2008; pp. 253–270. [CrossRef]
35. Sotiriadis, D.; Margaris, B.; Klimis, N.; Dokas, I.M. Seismic Hazard in Greece: A Comparative Study for the Region of East Macedonia and Thrace. *GeoHazards* **2023**, *4*, 239–266. [CrossRef]
36. Konti, C.; Vatalis, K.I. A Geospatial Assessment Framework of Seismic and Landslide Risk Using GIS. *Int. J. Appl. Geosp. Res.* **2022**, *13*, 22. [CrossRef]
37. Eskandari, R.; Scaioni, M. European Ground Motion Service For Bridge Monitoring: Temporal And Thermal Deformation Cross-Check Using Cosmo-Skymed Insar. *Int. Arch. Photogramm. Remote Sens. Spat. Inf. Sci.* **2023**, *48*, 1235–1241. Available online: https://isprs-archives.copernicus.org/articles/XLVIII-1-W2-2023/1235/2023/isprs-archives-XLVIII-1-W2-2023-1235-2023.html (accessed on 20 December 2024). [CrossRef]
38. Ferretti, A.; Passera, E.; Capes, R. *End-to-End Implementation and Operation of the European Ground Motion Service (EGMS): Product Description and Format Specification*; Technical Report EGMS-D3-PDF-SC1-2.0-007; European Environment Agency, Copernicus Land Monitoring Service: Copenhagen, Denmark, 2021.
39. Crosetto, M.; Solari, L.; Mróz, M. Pan-European deformation monitoring: The European Ground Motion Service. In Proceedings of the 5th Joint International Symposium on Deformation Monitoring (JISDM), Valencia, Spain, 20–22 June 2022; pp. 383–388. [CrossRef]
40. EGMS. Available online: https://egms.land.copernicus.eu (accessed on 15 June 2024).
41. Shahbazi, S.; Barra, A.; Navarro, J.A.; Crosetto, M. From EGMS Data to a Differential Deformation Map for Buildings at Continent Level. *Procedia Comput. Sci.* **2024**, *239*, 2150–2157. [CrossRef]
42. Hrysiewicz, A.; Khoshlahjeh Azar, M.; Holohan, E.P. EGMS-toolkit: A set of Python scripts for improved access to datasets from the European Ground Motion Service. *Earth Sci. Inform.* **2024**, *17*, 3825–3837. [CrossRef]
43. Crosetto, M.; Cuevas, M.; Balasis-Levinsen, J. Document Control Information Document Title Guidelines for EGMS Product Analysis Project Title EGMS Advisory Board. Available online: https://egms.land.copernicus.eu (accessed on 18 September 2024).
44. Google Earth. Available online: https://earth.google.com/web/ (accessed on 20 June 2024).
45. Farr, T.G.; Rosen, P.A.; Caro, E.; Crippen, R.; Duren, R.; Hensley, S.; Kobrick, M.; Paller, M.; Rodriguez, E.; Roth, L.; et al. The shuttle radar topography mission. *Rev. Geophys.* **2007**, *45*, 33. [CrossRef]
46. ESRI. Available online: https://pro.arcgis.com (accessed on 13 July 2024).
47. Svigkas, N.; Kiratzi, A.; Antonioli, A.; Atzori, S.; Tolomei, C.; Salvi, S.; Polcari, M.; Bignami, C. Earthquake source investigation of the Kanallaki, March 2020 Sequence (north-western Greece) based on seismic and geodetic data. *Remote Sens.* **2021**, *13*, 1752. [CrossRef]

48. Polcari, M.; Atzori, S.; Munafò, I. A new procedure for evaluating light-to-moderate earthquake location based on InSAR data and forward modeling tested on the Mediterranean area. *Sci. Remote Sens.* **2022**, *5*, 100057. [CrossRef]
49. Cigna, F.; Osmanoğlu, B.; Cabral-Cano, E.; Dixon, T.H.; Ávila-Olivera, J.A.; Garduño-Monroy, V.H.; DeMets, C.; Wdowinski, S. Monitoring land subsidence and its induced geological hazard with Synthetic Aperture Radar Interferometry: A case study in Morelia, Mexico. *Remote Sens. Environ.* **2012**, *117*, 146–161. [CrossRef]
50. Yang, Y.; Chen, Q.; Xu, Q.; Zhang, Y.; Yong, Q.; Liu, G. Coseismic surface deformation of the 2014 Napa earthquake mapped by Sentinel-1A SAR and accuracy assessment with COSMO-SkyMed and GPS data as cross validation. *Int. J. Digit. Earth* **2017**, *10*, 1197–1213. [CrossRef]
51. Wassie, Y.; Gao, Q.; Monserrat, O.; Barra, A.; Crippa, B.; Crosetto, M. Differential Sar Interferometry for The Monitoring of Land Subsidence Along Railway Infrastructures. *Int. Arch. Photogramm. Remote Sens. Spatial Inf. Sci.* **2022**, *43*, 361–366. [CrossRef]